Mars2020 entry shock layer thermochemical kinetics examined by MHz-rate laser absorption spectroscopy

Christopher Jelloian, Nicolas Minesi, R. Mitchell Spearrin, Augustin Tibère-Inglesse, Megan Macdonald, Brett Cruden

Mars2020 entry shock layer thermochemical kinetics examined by MHz-rate laser absorption spectroscopy

Christopher C. Jelloian*, Nicolas Q. Minesi †, and R. Mitchell Spearrin‡
University of California, Los Angeles (UCLA), Los Angeles, CA 90095, USA

Augustin Tibère-Inglesse§, Megan E. MacDonald¶, and Brett A. Cruden‖
NASA Ames Research Center, Moffett Field, CA 94035, USA

A mid-infrared laser absorption diagnostic was deployed to examine the evolution of thermophysical properties across a simulated Mars2020 shock layer in the Electric Arc Shock Tube (EAST) facility at NASA Ames. Rapid laser tuning techniques using bias-tee circuitry enabled quantitative temperature and number density measurements of CO_2 and CO with μs-resolution over a shock velocity range of 1.30 – 3.75 km/s. Two interband cascade lasers were utilized at 4.17 and 4.19 μm to resolve rovibrational CO_2 lines spanning across J" = 58 to J" = 140 in the asymmetric stretch fundamental bands. On test cases with enough energy to dissociate CO_2, a quantum cascade laser scanned multiple transitions of the CO fundamental bands near 4.98 μm. Results are compared to DPLR and LASTA simulations of the shock layer. A numerical simulation of the compressible boundary layer is used to account for measurement sensitivities to this flow feature in the EAST facility. Temperature and species transients are compared to multiple chemical kinetic models. The laser absorption data presented in this work can be used to refine the models used to simulate the aerothermal environment encountered during Mars entry.

I. Nomenclature

A_{21} = Einstein A coefficient of spontaneous emission

B_{21} = Einstein B coefficient of stimulated emission

B_{12} = Einstein B coefficient of absorption

$E_{\mathrm{rot},i}$ = energy of rotational level i

$E_{\mathrm{vib},i}$ = energy of vibrational level i

*Ph.D. Candidate, Mechanical and Aerospace Engineering Department, Member AIAA. Corresponding author: cjelloian@g.ucla.edu
†Postdoctoral Researcher, Mechanical and Aerospace Engineering Department, Member AIAA.
‡Associate Professor, Mechanical and Aerospace Engineering Department, Member AIAA.
§Postdoctoral Scholar, Aerothermodynamics Branch, Member AIAA
¶Senior Aerospace Engineer, Thermophysics Facilities Branch, Member AIAA
‖Senior Research Scientist, Aerothermodynamics Branch, AIAA Associate Fellow
Presented as Paper 2023-0960 at the AIAA SciTech 2023 Forum, January 23-27, 2023 in National Harbor, MD

c = speed of light

c_p = specific heat at constant pressure

c_2 = second radiation constant

D_{rot} = rotational degrees of freedom

g_i = degeneracy of level i

h = Planck's constant

h_0 = stagnation enthalpy

h_f^0 = enthalpy of formation

I_t = transmitted light intensity

I_0 = incident light intensity

J'' = lower state rotational quantum number

k = thermal conductivity

L = pathlength

M = molecular weight

n = collisional broadening coefficient of temperature dependence

n_A = number density of absorbing species A

n_i = population of level i

P = pressure

R = gas constant

Q = partition function

S_j = linestrength of transition j

T_{tr} = translational temperature

T_{rot} = rotational temperature

T_{vib} = vibrational temperature

U_{is} = incident shock wave velocity

u = flow velocity in the x direction

v = flow velocity in the y direction

v'' = lower state vibrational quantum number

X = mole fraction

α = absorbance

μ = dynamic viscosity

ν_0 = transition wavenumber center

$\Delta\nu_C$ = collisional (Lorentzian) FWHM

$\Delta\nu_D$ = Doppler (Gaussian) FWHM

δ_{99} = boundary layer thickness

ϕ = lineshape function

γ_{A-B} = collisional broadening coefficient

$\mathcal{A}_i$ = absorbance area of transition i

II. Introduction

The Mars2020 mission successfully landed the Perseverance rover within the Jezero crater at the Octavia E. Butler landing site on February 18, 2021. The aeroshell of the Mars2020 mission was instrumented with the MEDLI2 sensor suite [1–3] to conduct measurements of the aerothermal environment upon entry, descent, and landing (EDL). Temperatures were recorded at multiple locations via thermocouples. Total heat flux was recorded on the backshell by two sensors (MEDTHERM, Model 22171-01KS) and the backshell radiative heating component was measured via a radiometer (MEDTHERM, Model 22160-22KS-1.410). Figure 1 shows the backshell instrumentation and compares the flight data to the NASA simulations [1]. The total heat flux measured during the mission is generally well captured

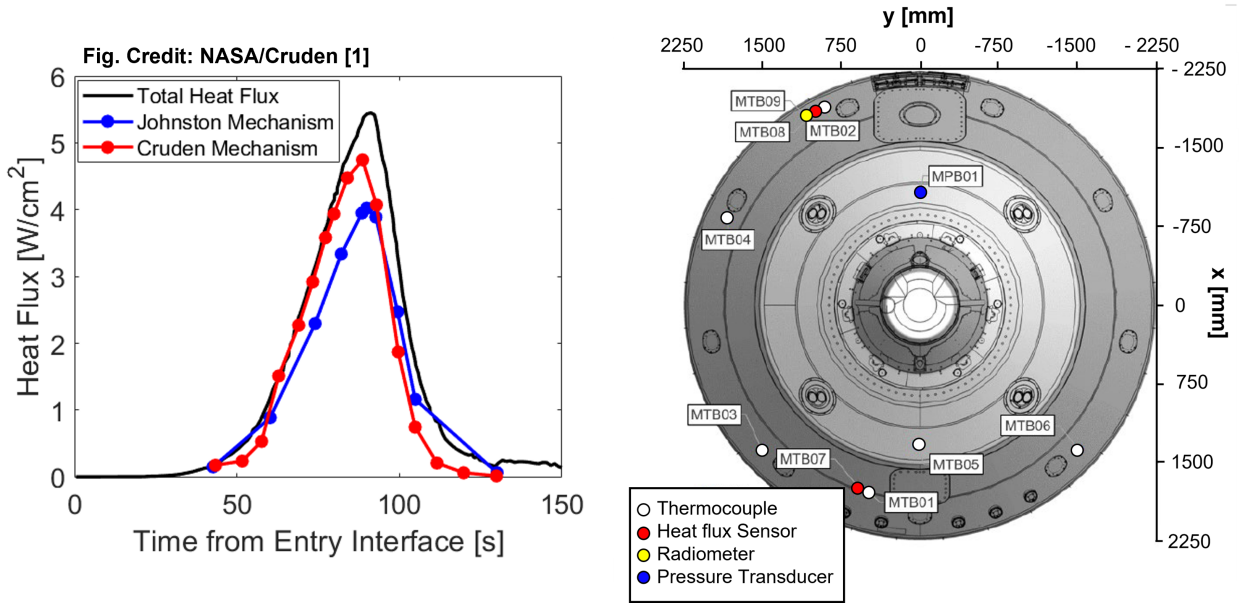

Fig. 1 MEDLI2 flight data (total heat flux) compared to the radiative heat flux predicted by the Cruden [4, 5] and Johnston [6] mechanisms (left). Backshell measurement locations of the MEDLI2 sensor suite (right). Figure reproduced from [1–3, 7].

by the NASA Cruden and Johnston models [4–6], with under prediction at the peak due to a small contribution of convective heating. The Cruden mechanism matches the flight data well at early test times, and the Johnston mechanism performs better at later test times. The test series (64A) at the Electric Arc Shock Tube (EAST) facility at NASA

Ames was conducted to investigate the Mars2020 conditions experienced by the MEDLI2 sensor in order to reduce uncertainties in the models. For that purpose, the EAST facility was equipped with several mid-infrared lasers for absorption spectroscopy measurements of temperature and number density of CO, and CO_2 [8, 9]. In parallel, multiple spectrometers recorded emission signals to obtain the spectral radiance of the shock layer. This work presents the laser absorption spectroscopy (LAS) results whereas a companion paper [10] details the optical emission spectroscopy (OES) results and compares the two techniques.

Prior experimental work examining non-equilibrium of CO_2 and CO at entry conditions has been conducted by various groups using a multitude of optical diagnostic techniques. Select relevant works have deployed (FTIR) absorption spectroscopy [11] and calibrated emission spectroscopy techniques [4, 12–15] in both plasma torches and shock tube facilities. Specifically, Klarenaar et al. [11] captured non-equilibrium infrared spectra of CO_2 and CO via an FTIR and infer rotational temperature as well as mode-specific vibrational temperatures in a glow discharge. Utilizing electronic excitation to initiate CO_2 dissociation is a fundamentally different excitation mechanism than that experienced during Mars entry. In the plasma torch, the energy flows from the electrons to the translational energy mode. In the planetary entry case, energy flows from translational energy mode to the vibrational and electronic modes. Even though the excitation mechanisms are different, the plasma torch experiments are very valuable in probing energy pathways and rates of energy exchange within and in between molecules. Shock tube studies of CO_2 provide a means to create very similar thermochemical kinetics to that experienced in flight by Mars entry vehicles [16]. The NASA Ames EAST facility has utilized both calibrated emission [4, 17] and laser absorption techniques [18] to measure the translational, rotational, and vibrational temperature of the lab-simulated Mars entry flow. Translational temperature was determined from the laser absorption measurements of the Doppler width of a CO spectral feature (R(0, 51)) near 4.36 μm. Rotational and vibrational temperatures were determined from C_2 emission near 385 nm. These shock tube measurements are used to help inform and validate reacting computational fluid dynamics models [19, 20] and radiation codes [20, 21] used by NASA in thermal protection system design. Additionally, these measurements and the results presented in this current work can be used by other groups [22–25] who have worked to build non-equilibrium state-to-state models of CO_2.

This paper presents the laser absorption methods and the novel dataset generated by such methods in the Mars2020 ground test series 64A at the NASA EAST facility. The absorption spectroscopy theory and spectral line selection are first described. The experimental setup on the EAST facility and test conditions relevant to the MEDLI2 sensor are then detailed. A compressible boundary layer analysis of the flow inside EAST is presented and utilized to adjust the measurement interpretation. The spectral fitting method and a subset of experimental results are described and compared to NASA CFD models. Following discussion of the results and associated conclusions, an uncertainty analysis is presented in the appendix as well as a full test catalogue of additional laser absorption data to be published on data.nasa.gov.

III. Methods and Theory

Laser absorption spectroscopy (LAS) is utilized to infer temperatures and number density of CO_2 and CO from spectrally-resolved light attenuation in the mid-wave infrared. LAS theory is well-detailed in literature [26], and key governing equations are briefly discussed in this section for context and nomenclature definition. The Beer-Lambert law, shown in Eq. 1, relates the spectral absorbance α at frequency ν to thermophysical gas properties (temperature, number density, velocity, etc.) via incident and transmitted light intensities, I_0 and I_t, respectively.

$$\alpha(\nu) = -\ln\left(\frac{I_t}{I_0}\right)_\nu = S_j(T_{\text{rot}}, T_{\text{vib}}) n_A L \phi_j(\nu, T_{\text{tr}}, P, X_A) \tag{1}$$

Here, n_A [molec $\cdot$ cm^{-3}] is the number density of the absorbing species A, L [cm] is the pathlength, $S_j(T_{\text{rot}}, T_{\text{vib}})$ [cm^{-1}/(molec $\cdot$ cm^{-2})] is the linestrength of rovibrational transition j at rotational temperature T_{rot} [K] and vibrational temperature T_{vib} [K], and $\phi_j(\nu, T_{\text{tr}}, P, X_A)$ [cm] is the lineshape function.

In this study, ϕ_j is resolved via scanned-wavelength laser absorption spectroscopy. Each individual lineshape (ϕ_j) can be fit assuming a Voigt profile, without enforcing a single temperature or number density over all the features. Through analysis of the resulting absorbance area ratios, a temperature and number density can be determined. To correctly apply this method it is important to consider sensitivity of the fitted features to non-ideal effects such as a cool boundary layer, or by neighboring absorbance features. When the features are found to be sensitive to these experimental non-idealities, sequential fitting techniques or numerical models should be used to properly interpret the data, see Section III.C.

The Voigt lineshape includes the Doppler and collisional broadening effects of the features as a convolution of Gaussian and Lorentzian profiles. The value of ϕ_j at the transition linecenter $\nu_{j,0}$ is expressed in Eq. 2, where a is the spectral damping parameter and $\Delta\nu_D$ [cm^{-1}] and $\Delta\nu_C$ [cm^{-1}] are the Doppler and collisional linewidth contributions, respectively.

$$\phi_j(\nu_{j,0}) = \frac{2}{\Delta\nu_D}\sqrt{\frac{\ln 2}{\pi}}\exp\left(a^2\right)[1 - \text{erf}(a)] \tag{2}$$

$$a = \frac{\sqrt{\ln 2}\Delta\nu_C}{\Delta\nu_D} \tag{3}$$

The Doppler linewidth depends on translational temperature T_{tr}, the molecular weight M [g/mol] of the absorbing species, and the transition linecenter $\nu_{j,0}$ [cm^{-1}] as indicated in Eq. 4.

$$\Delta\nu_D = \nu_{J,0}(7.1623 \times 10^{-7})\sqrt{\frac{T_{\text{tr}}}{M}} \tag{4}$$

Collisional linewidth scales with pressure and the mole fraction weighted broadening coefficient of collision partner B with absorbing molecule A, as shown in Eq. 5. Additionally, the broadening coefficient (γ_{A-B}) is typically modeled by

implementing a power law, as shown in Eq. 6, where T_0 [K] is a reference temperature and n is the temperature exponent.

$$\Delta\nu_C = P \sum_B X_B 2\gamma_{A-B} \tag{5}$$

$$\gamma_{A-B}(T_{\mathrm{Tr}}) = \gamma_{A-B}(T_0)\left(\frac{T_0}{T_{\mathrm{Tr}}}\right)^n \tag{6}$$

$$\int_{-\infty}^{\infty} \alpha(\nu)d\nu = \mathcal{A}_j = S_j(T_{\mathrm{rot}}, T_{\mathrm{vib}})n_A L \tag{7}$$

Temperature, number density and pathlength information is contained in the absorbance area of each transition (Eq. 7). Absorbance area ratios, as shown in Eq. 8, are independent of number density and optical pathlength, reducing to ratios of linestrengths which are only a function of temperature. Rovibrational line ratios can be written as a function of multiple temperatures (rotation and vibration) assuming a Boltzmann distribution. The linestrength, S_j, expression as shown in Eq. 9, accounts for stimulated emission.

$$\frac{\mathcal{A}_1}{\mathcal{A}_2} = \frac{S_1(T_{\mathrm{rot}}, T_{\mathrm{vib}})}{S_2(T_{\mathrm{rot}}, T_{\mathrm{vib}})} \tag{8}$$

$$S_j = (n_1 B_{12} - n_2 B_{21})\frac{h\nu}{c} \tag{9}$$

B_{12} and B_{21} [$\mathrm{cm^3/(erg{\cdot}s^2)}$] are the Einstein coefficients for absorption and stimulated emission, which are calculated from the Einstein A coefficient (A_{21} [$\mathrm{s^{-1}}$]) tabulated in HITEMP [27], h [$\mathrm{(cm^2{\cdot}g)/s}$] is Planck's constant, ν [$\mathrm{cm^{-1}}$] is the wavenumber of the transition, c [cm/s] is the speed of light, n_1 and n_2 [$\mathrm{molec/cm^3}$] are the populations of the lower and upper levels respectively. By assuming separable Boltzmann populations over rotation and vibration, Eq. 9 can be rewritten as Eq. 10, where g_2 is the upper-level degeneracy of the transition, $E_{\mathrm{rot},1}$ and $E_{\mathrm{vib},1}$ [$\mathrm{cm^{-1}}$] are the rotational and vibrational energies of the lower state, $E_{\mathrm{rot},2}$ and $E_{\mathrm{vib},2}$ [$\mathrm{cm^{-1}}$] are the rotational and vibrational energies of the upper state, c_2 (1.4388 [cm·K]) is a radiation constant for unit compatibility, and Q_{rot} and Q_{vib} are the partition functions of rotation and vibration taken from NEQAIR [28].

$$S_j = \frac{A_{21}g_2}{8\pi\nu^2 c Q_{\mathrm{rot}}(T_{\mathrm{rot}})Q_{\mathrm{vib}}(T_{\mathrm{vib}})}\left[\exp\left(\frac{-c_2E_{\mathrm{rot},1}}{T_{\mathrm{rot}}}\right)\exp\left(\frac{-c_2E_{\mathrm{vib},1}}{T_{\mathrm{vib}}}\right) - \exp\left(\frac{-c_2E_{\mathrm{rot},2}}{T_{\mathrm{rot}}}\right)\exp\left(\frac{-c_2E_{\mathrm{vib},2}}{T_{\mathrm{vib}}}\right)\right] \tag{10}$$

It is important to note that CO_2 has three vibrational modes: symmetric stretch, doubly degenerate bending, and asymmetric stretch which may be at separate temperatures. In this work, a single vibrational temperature is assumed over all the vibrational modes.

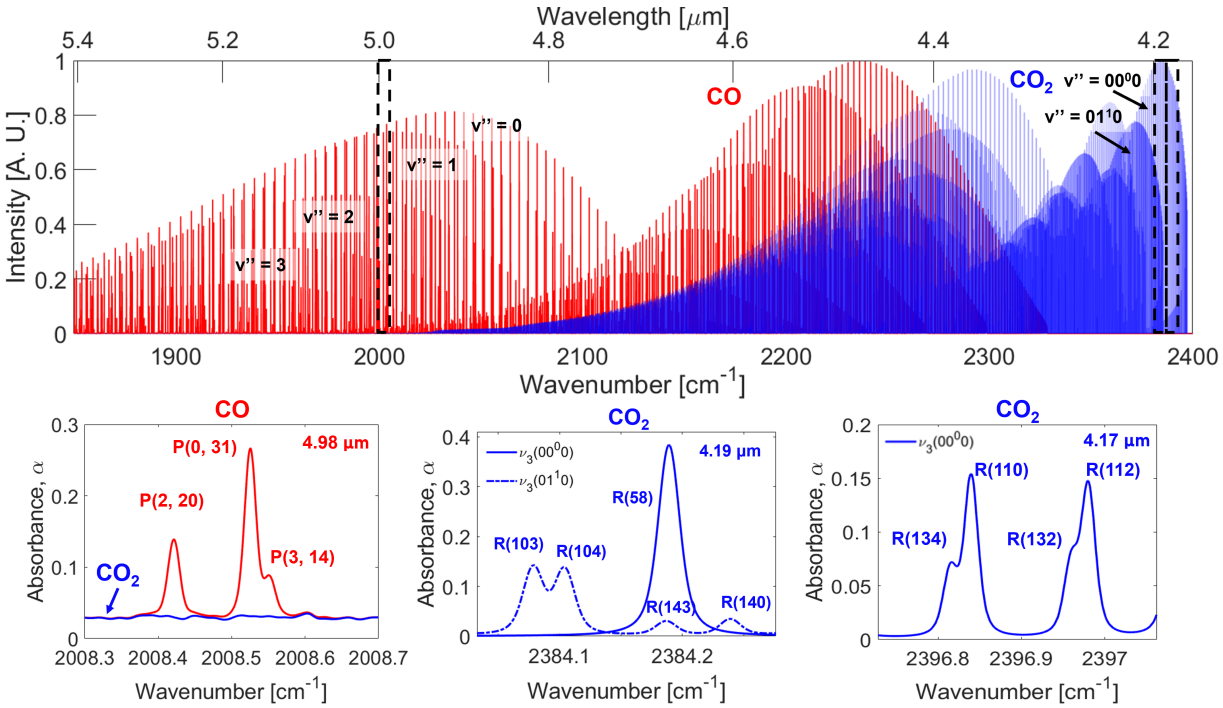

Fig. 2 Line survey of the fundamental bands of CO and the asymmetric stretch fundamental bands of CO_2 from 4.2 - 5.4 μm (top) Simulated spectrum of resolved transitions of CO (bottom left), and CO_2 (bottom middle and bottom right) using the HITEMP database [27]. Vibrational lower state of CO_2 is denoted with the solid/dashed lines at 4.19 and 4.17 μm. CO_2 absorption at 4.98 μm is from many different vibrational bands and the CDSD database [29] was used at this wavelength. Spectra are simulated at 3300 K, 0.3 atm, 10.16 cm optical pathlength, 0.1 mole fraction of CO_2, and 0.02 mole fraction of CO. At 4.98 μm, the CO spectrum (bottom left) is presented as a sum with the CO_2 baseline.

A. Line selection

In this work, a total of twelve spectral transitions (see Table 1) are targeted near 4.17, 4.19, and 4.98 μm to resolve temperatures and number densities of both CO_2 and CO. These lines were selected for strong absorbance signals over a wide range of temperatures with sufficient spectral isolation to enable resolution of individual integrated areas, and large energy level spacing making the measurement sensitive to temperature.

The carbon dioxide molecule possesses multiple modes of vibration represented within the target spectrum. The fundamental vibrational frequencies of CO_2 are: symmetric stretch (ν_1, 1334 cm^{-1}), doubly degenerate bending (ν_2, 667 cm^{-1}), and asymmetric stretch (ν_3, 2349 cm^{-1}). In this study, the CO_2 spectra are from the strong absorption region near 4.3 μm which corresponds to the fundamental asymmetric stretch bands (ν_3) where $\Delta v_3 = 1$. The fundamental asymmetric stretch bands can be distinguished by their lower vibrational levels, denoted with vibrational quantum numbers $v_1 v_2^{l_2} v_3$. When the bending mode v_2 is excited, there are $v_2 + 1$ sublevels due to rotation around the O-C-O molecular axis. l_2 quantifies the projection of the resultant vibrational angular momentum on the quantization axis [30]. Levels with $l_2 > 0$ are doubly degenerate. Within the vibrational bands, rotational lines are indicated as X(J") where X is the branch (R, P, or Q) describing an increase, decrease, or no change in rotational quantum number, with J"

being the lower state rotational assignment. In this work, we probe two ν_3 fundamental bands, notated as $\nu_3(00^00)$ and $\nu_3(01^10)$, and several rotational lines within the R branch of these bands ranging from J" = 58 to J" = 140. The large range of rotational quantum numbers in this domain are associated with the proximity to the R-branch bandheads which also provide good isolation from ambient CO_2 interference [31]. The target absorption transitions of CO_2 are shown in Fig. 2. The two bands utilized in this study are distinguished by lower vibrational energy level of the bending mode (differentiated by the solid and dashed lines in Fig. 2: solid for the ground state, 00^00, and dashed for the first excited bending mode, 01^10), as both bands originate from the ground vibrational state of the symmetric (v_1 = 0) and asymmetric (v_3 = 0) stretch. The R(58) line of the $\nu_3(00^00)$ band and the R(103), R(104), and R(140) transitions of the $\nu_3(01^10)$ band are targeted for measurement by an interband cascade laser (ICL) centered near 4.19 μm. A second ICL at 4.17 μm is used to probe the R(110), R(112), R(132), and R(134) lines in the $\nu_3(00^00)$ band. This multi-laser sensing strategy reduces uncertainty in the CO_2 temperature measurement where the multiple lines can be fit using a Boltzmann plot (discussed later) and the maximum energy difference is $\Delta E''$ = 7004 cm^{-1}. At some low-temperature conditions (~<2700 K), the $\nu_3(00^00)$ R(58) feature is optically thick and the temperature sensitivity is mainly driven by the $\nu_3(01^10)$ R(103) and $\nu_3(01^10)$ R(140) line pair with $\Delta E''$ = 3502 cm^{-1}.

Table 1 Spectral features and their corresponding rotational and vibrational lower state energies probed in this work. $E''_{total} = E''_{vib} + E''_{rot}$

Molecule	Linecenter [cm^{-1}]	Line Label	E''_{vib} [cm^{-1}]	E''_{rot} [cm^{-1}]	E''_{total} [cm^{-1}]
CO	2008.42	P(2, 20)	4260	792	5052
CO	2008.53	P(0, 31)	0	1901	1901
CO	2008.55	P(3, 14)	6350	392	6742
CO_2	2384.08	$\nu_3(01^10)$ R(103)	667	4169	4836
CO_2	2384.10	$\nu_3(01^10)$ R(104)	667	4257	4924
CO_2	2384.19	$\nu_3(01^10)$ R(143)	667	7987	8654
CO_2	2384.19	$\nu_3(00^00)$ R(58)	0	1334	1334
CO_2	2384.24	$\nu_3(01^10)$ R(140)	667	7671	8338
CO_2	2396.81	$\nu_3(00^00)$ R(134)	0	7015	7015
CO_2	2396.84	$\nu_3(00^00)$ R(110)	0	4745	4745
CO_2	2396.96	$\nu_3(00^00)$ R(132)	0	6810	6810
CO_2	2396.98	$\nu_3(00^00)$ R(112)	0	4917	4917

For CO, the line identifier B(v'',J'') indicates the branch (R or P) and lower state vibrational and rotational quantum numbers. As shown in Fig. 2, the P(2, 20), P(0, 31), and P(3, 14) lines are targeted for measurement. This line selection has been used in previous work and demonstrated high sensitivity to temperature with $\Delta E''$ = 4841 cm^{-1} [8, 32, 33].

B. Experimental Setup and Test Conditions

To resolve the spectral features described above in Sec. III.A, two beam paths are utilized with three lasers as shown in Fig. 3. Two NanoPlus interband cascade lasers (ICLs) were utilized near 4.19 and 4.17 μm to measure CO_2 transitions and one Alpes quantum cascade laser was utilized near 4.98 μm to measure CO spectra. The lasers were controlled with Arroyo 6300 series laser controllers and SRS DS345 function generators. The lasers were scanned at 1 MHz with a bias tee control circuit utilizing square waves to maximize tunability given detection bandwidth constraints[34]. The light is focused into InF_3 single mode fibers and mounted directly to the EAST test section. The light is collimated upon exiting the fiber and pitched across the shock tube's 10.16 cm pathlength. High bandwidth (~200 MHz) AC coupled photovoltaic Vigo detectors (PVI-4TE-5-1x1) are mounted in-line approximately 4 inches from the optical port and contain an iris, bandpass filter, and focusing lens to reduce thermal emission without sacrificing laser signal-to-noise ratio. For shock velocities above ~2.7 km/s, the temperature is high enough and the kinetics are sufficiently fast to dissociate CO_2 and form CO in detectable quantities during the test time. In these cases, the 4.17-μm ICL laser used for CO_2 is replaced by a quantum cascade laser (QCL) scanning at 2008 cm^{-1} (= 4.98 μm) to monitor CO formation. A 2-inch germanium etalon with a free spectral range of 0.024 cm^{-1} is used to convert light intensity signals from the time domain to the wavenumber domain. The etalon signals were recorded for each laser immediately before tests. A 1 GHz bandwidth Tektronix DPO5014B scope was used to record the light intensity signals.

The EAST facility at NASA Ames was used to generate the conditions of interest for this study. This facility is well documented in literature [35] and is briefly described below. A 1.25 MJ capacitor bank supplies energy for the electric arc driver. The facility is capable of generating incident shock velocities up to 46 km/s through the 30-foot driven section though in this study the shock velocities ranged from 1.30 - 3.75 km/s. During the test series 64A, 53 tests were performed to simulate entry in the Martian atmosphere (95.4% CO_2, 2.6% N_2, 2.0% Ar) [36]. After each run, the facility was cleaned and then turbopumped overnight. Three primary fill pressures were used: 1.09, 1.49, and 1.99 Torr to produce a similar shock to that experienced by the MEDLI2 sensor at different points in the Mars2020 entry trajectory. These fill pressures were determined based on the shock tube informed bias method developed by Johnston [16]. A few tests at 0.49 Torr were conducted to observe CO_2 vibrational relaxation and at 8.90 Torr to investigate CO formation at lower shock velocities.

C. Boundary Layer Analysis

Shock tubes are prone to boundary layer formation behind incident shock waves, particularly for test mixtures that involve a large fraction of polyatomic gases [37, 38], as was the case for this test series. Line-of-sight or path-integrated measurements of gas properties can be biased by such boundary layers, motivating the detailed accounting presented in this work. Specifically, the CO_2 absorbance signal was found to be sensitive to a boundary layer formed at certain conditions in this study (discussed further in the results). Numerical methods were used to estimate the boundary layer

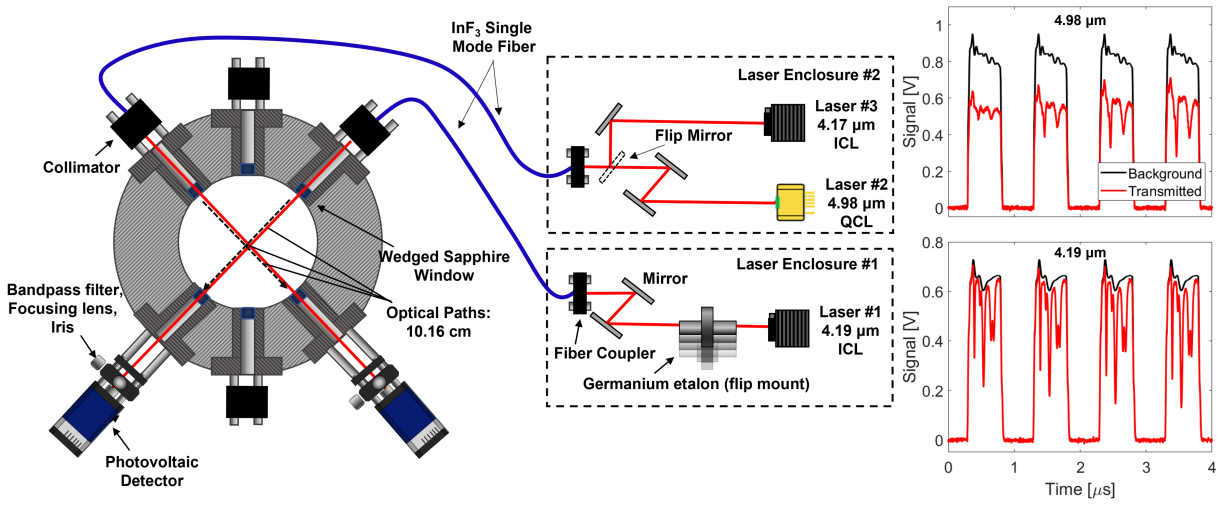

Fig. 3 Optical setup on the EAST facility. Two laser enclosures contain the beam and couple the light into InF_3 single mode fibers. The 4.17-μm ICL laser or the 4.98-μm QCL laser were used depending on the expected shock speed (left). Representative background and transmitted light intensity signals for the first 4 μs of a test (right).

and show its effect on inferred temperature and number density over the range of relevant conditions. The compressible boundary layer in a shock tube is well described by Mirels' theory [39] and the governing equations are shown in Eqs. 11 - 14.

$$\frac{\partial(\rho u)}{\partial x} + \frac{\partial(\rho v)}{\partial y} = 0 \qquad \text{(Mass)} \tag{11}$$

$$\rho\left(u\frac{\partial u}{\partial x} + v\frac{\partial u}{\partial y}\right) = -\frac{\partial p}{\partial x} + \frac{\partial}{\partial y}\left(\mu\frac{\partial u}{\partial y}\right) \qquad \text{(x - momentum)} \tag{12}$$

$$\frac{\partial p}{\partial y} = 0 \qquad \text{(y - momentum)} \tag{13}$$

$$\rho c_p\left(u\frac{\partial T}{\partial x} + v\frac{\partial T}{\partial y}\right) = -u\frac{\partial p}{\partial x} + \frac{\partial}{\partial y}\left(k\frac{\partial T}{\partial y}\right) + \mu\left(\frac{\partial u}{\partial y}\right)^2 \qquad \text{(Energy)} \tag{14}$$

ρ is the density, u and v are the velocity in the flow (x) and wall normal (y) directions, p is the pressure, T is the temperature, μ is the dynamic viscosity, c_p is the specific heat at constant pressure, and k is the thermal conductivity of the gas. Dynamic viscosity and thermal conductivity are calculated at elevated temperatures via Sutherland's law [40] as shown in Eqs. 15 and 16.

$$\frac{\mu}{\mu_0} = \left(\frac{T}{T_0}\right)^{\frac{3}{2}} \frac{T_0 + S_\mu}{T + S_\mu} \tag{15}$$

$$\frac{k}{k_0} = \left(\frac{T}{T_0}\right)^{\frac{3}{2}} \frac{T_0 + S_k}{T + S_k} \tag{16}$$

Sutherland's law is based on kinetic theory, and has been shown to be accurate over a wide range of temperatures for air and is commonly used in hypersonics CFD programs. For the simulation of the compressible boundary layer in this study, the gas viscosity is assumed to be that of CO_2, as it is the major constituent (95.4%) of the mixture. Table 1-2 and 1-3 of [40] list the viscosity of CO_2 as 1.370×10^{-5} [(N·s)/m^2] and thermal conductivity of CO_2 as 0.0146 [W/(m·K)] at the reference temperature of 273 K. Additionally, the Sutherland constants for CO_2 are listed as S_μ = 222 K and S_k = 1800 K.

Mirels provides a similarity variable, η, for solving the compressible boundary layer equations as shown in Eq. 17.

$$\eta = \sqrt{\frac{1}{2}\frac{u_e \rho_e}{x \mu_e}} \int_0^y \frac{T_e}{T} dy \tag{17}$$

In shock fixed coordinates, the boundary conditions of Mirels are shown in Eq. 18 - 22.

$$u(x, 0) = -U_{is} \tag{18}$$

$$v(x, 0) = 0 \tag{19}$$

$$T(x, 0) = T_w \tag{20}$$

$$u(x, \infty) = u_2 \tag{21}$$

$$T(x, \infty) = T_2 \tag{22}$$

The velocity in the x direction at the wall is determined from the no-slip condition. The y velocity at the wall is zero. The wall temperature is held fixed and the velocity determined from the normal shock relations is enforced at $\eta = \infty$. The temperature at $\eta = \infty$ is expected to be lower than that predicted from normal shock relations due to dissociation and was determined from CFD. The temperature uncertainty in the boundary condition at $\eta = \infty$ is expected to have a minimal effect on boundary layer size and CO_2 absorption, as discussed later in this section.

There are multiple ways to numerically solve this system of equations using modern methods. For this study, the solution method of Oz et al. [41] for the compressible boundary layer of air over a flat plate was combined with Mirels' theory to estimate the compressible boundary layer properties behind a stationary shock wave in a CO_2 test gas. A 4th order Runge-Kutta method is utilized with Newton's iteration method [41] to close the system of equations and allow a numerical solution. The freestream velocity and temperature ($\eta = \infty$) are used as the convergence criteria. Once the similarity solution is obtained, Eq. 23 is applied to transform η back to x and y coordinates.

$$y\sqrt{\frac{1}{2}\frac{u_e \rho_e}{x \mu_e}} = \int_0^\eta \frac{T}{T_e} d\eta \tag{23}$$

A typical boundary layer temperature profile is presented in Fig. 4. The temperature trends from the wall temperature ($\sim$ 297 K) to the core flow temperature (2000 – 3500 K) within the boundary layer thickness (see the δ_{99} curve in Fig.

4). Additionally, the number density is inversely related to the temperature profile, resulting in approximately ten times more CO_2 near the wall than in the freestream (core) flow. This boundary layer simulation result was found to be within 10% of the boundary layer thickness estimated in the LASTA code [42] when comparing up to 10 cm behind the shock front. LASTA [42] utilizes a slightly different approach in the estimation of the boundary layer though it is still based on Mirels' theory.

The molecular absorbance in the boundary layer can be estimated at the measured locations behind the incident shock wave by integrating the incremental absorbance associated with the profiles of temperature and density in this relatively thin (1–2 mm) region. This simulated boundary layer absorbance, in Fig. 4, is then subtracted from the line of sight (LOS) measurement, which is then refit to estimate a new temperature and number density of CO_2. The low temperature, high number density region is the primary contributor to the boundary layer absorbance signal, specifically affecting the $\nu_3(00^00)$ R(58) feature whose linestrength peaks around 800 K. Figure 5 presents the simulated area difference [%] of the CO_2 spectral line as a function of the temperature at $\eta = \infty$, see Eq. 24 where $\mathcal{A}_{\text{LOS}}$ and $\mathcal{A}_{\text{Core}}$ are the line areas calculated with and without including the presence a boundary layer.

$$\%\text{Area Change} = \frac{100 \times |\mathcal{A}_{\text{Core}} - \mathcal{A}_{\text{LOS}}|}{\mathcal{A}_{\text{Core}}} \tag{24}$$

The weak effect of the boundary layer on lines with $J'' > 58$ is due to the absence of these features in the low-temperature spectra of the boundary layer.

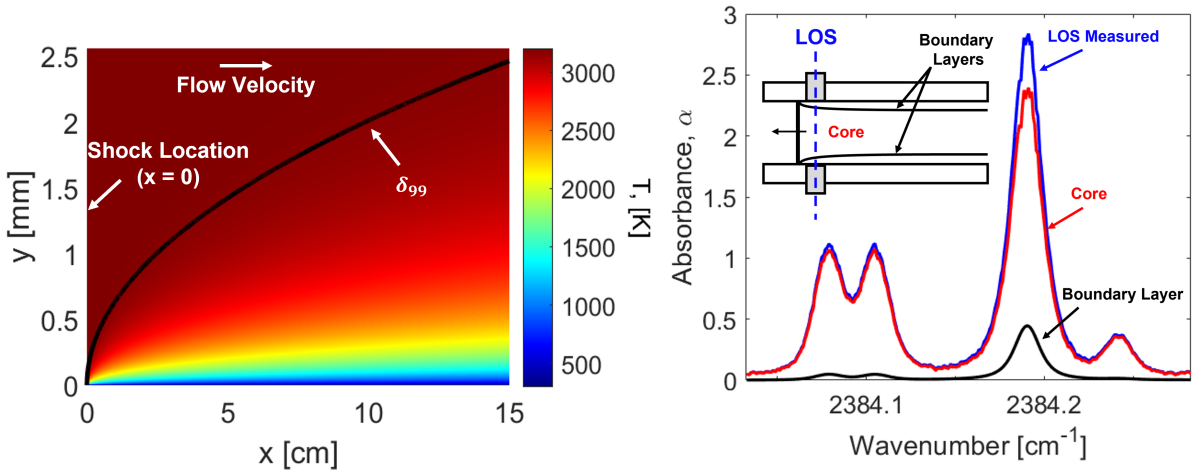

Fig. 4 (left) Simulated compressible boundary layer temperature profile. The shock location, δ_{99} thickness and freestream flow direction are highlighted. The no slip condition is enforced at the wall (y = 0). (right) Absorbance signals from the line of sight (blue), core (red), and boundary layer (black) estimated from a similarity solution of the boundary layer profile.

In summary, the $\nu_3(00^00)$ R(58) absorbance signal has been shown to be sensitive to a boundary layer affecting ~2%

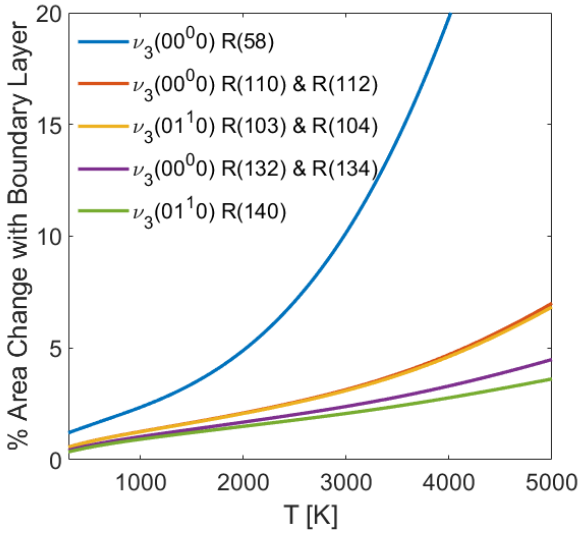

Fig. 5 Sensitivity of path-integrated line intensity (measured absorbance area) to a representative simulated cold boundary layer (≈1 mm) in the EAST facility assuming a similarity solution of a 2.96 km/s shock with a fill pressure of 1.49 Torr and scaled by variable core temperature (T).

of the 10.16 cm total pathlength at velocities > 2.5 km/s, and is accounted for in the results presented in Sec. IV. At velocities below 2.5 km/s, the inferred temperature and number densities are shown not to be sensitive to the boundary layer. Accounting for a simulated laminar boundary layer generally increases the LAS CO_2 temperature typically less than 5% and increases the inferred number density on the order of 10% at velocities near 3.0 km/s.

D. Spectrum Fitting Method

Absorption lines were fit assuming Voigt profiles allowing the collision width and absorbance area of each transition to float. Sample Voigt fits are shown below in Figs. 6 - 8 for each wavelength. The boundary layer correction has been applied on tests with shock velocities > 2.5 km/s, as lower velocities have been shown to be unaffected by the boundary layer (see the Appendix). The CO_2 spectrum at 4.19 μm is sequentially fit to recover individual line areas and mitigate the effect of an optically thick and blended $\nu_3(00^00)$ R(58) feature, with the approach shown previously to yield accurate results [9]. In the fitting routine, the $\nu_3(01^10)$ R(143) line area (that is blended with the $\nu_3(00^00)$ R(58) feature) is estimated as a fraction of the measured area of the neighboring $\nu_3(01^10)$ R(140) feature based off of the temperature-dependent linestrength model. The recovered line areas are utilized in the Boltzmann plot method described below to infer temperature and number density. Fitting the CO spectrum (and recovering respective line areas) at 4.98 μm is complicated by an underlying spectrum from high vibrational states of CO_2. To correct for this CO_2 interference, the local CO_2 spectrum at 4.98 μm was determined from observation of the absorption cross-sections at early test times (with negligible CO formation) over a range of temperatures investigated in this study. The initial absorbance associated with the cross-section was normalized ($\alpha_{CO2,normalized}$) and allowed to scale (by factor C in Eq.

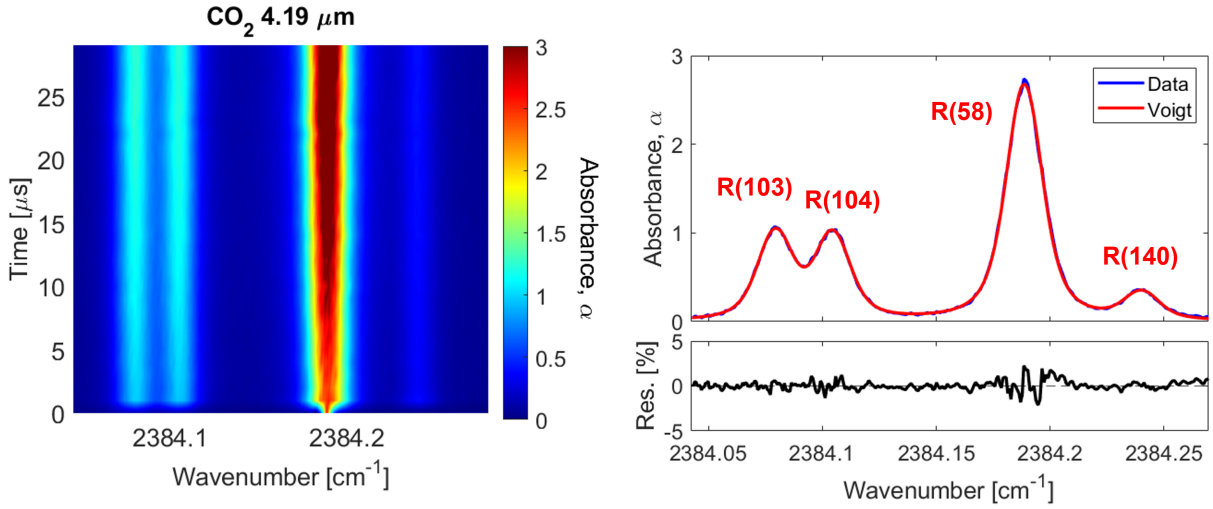

Fig. 6 (left) Absorbance vs wavenumber and time for CO spectrum at 4.19 μm. (right) Representative Voigt fit of spectrum at t = 7 μs.

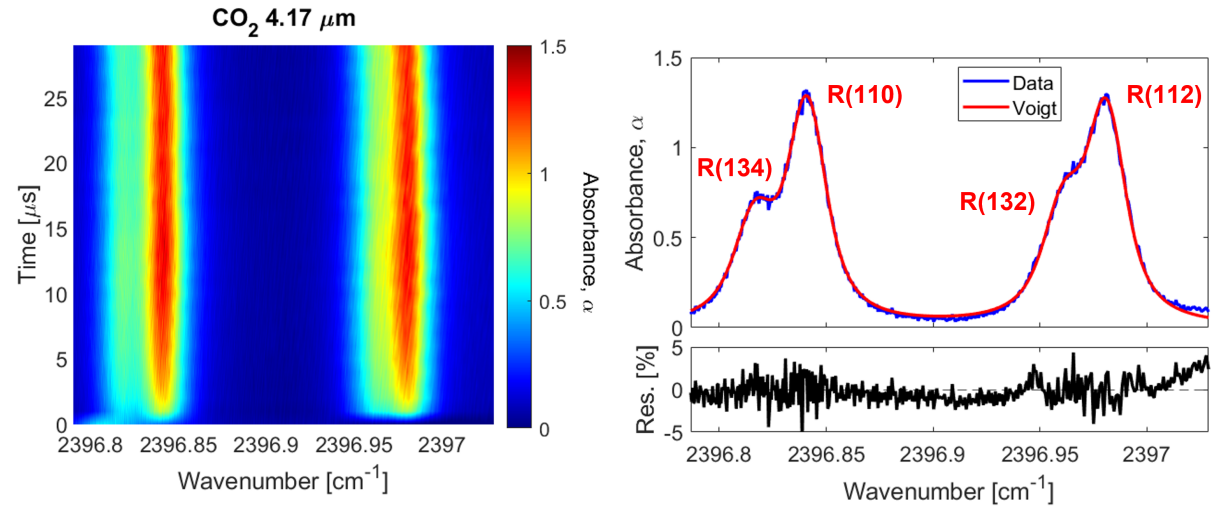

Fig. 7 (left) Absorbance vs wavenumber and time for CO_2 spectrum at 4.17 μm. (right) Representative Voigt fit of spectrum at t = 11 μs.

25) during the fit to allow for variable composition.

$$\alpha_{4.98} = C * \alpha_{CO2,normalized} + \alpha_{CO} \tag{25}$$

Example fits of the respective CO and CO_2 spectra and representative time histories of absorbance behind an incident shock wave are shown in Figs. 6 - 8. The rovibrational states that were probed in this study generally were populated very rapidly behind the shock front and this resulted in high SNR throughout most of the test time, with spectra resolved at 1 MHz. Signals are typically increasing throughout the test times due to two effects. First, The CO signal increases primarily as CO is formed. Second, as the gas cools due to dissociation, the CO_2 signal increases as the relatively low

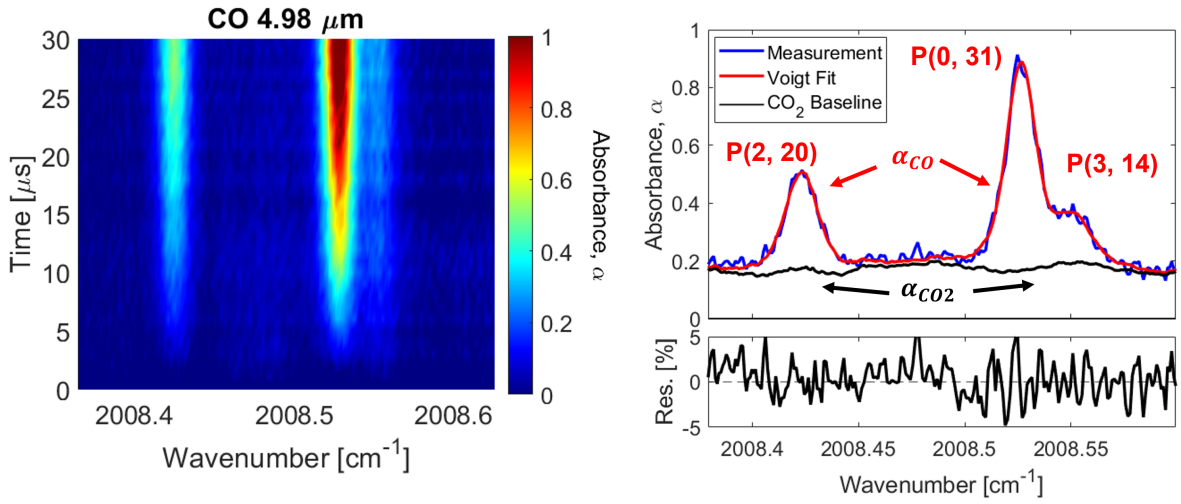

Fig. 8 (left) Absorbance vs wavenumber and time for CO spectrum at 4.98 μm. (right) Representative Voigt fit of spectrum at t = 15 μs.

lying energy states resolved in this work become more populated. The transients seen in the absorbance signal imply changing temperature and composition throughout the test.

A multi-line Boltzmann plotting and regression method is used to determine the temperature as a function of time behind each shock. This largely follows the analysis of Minesi et al. [43] who details the derivation of the key expressions given in Eqs. 26 and 27.

$$\ln\left(\frac{\mathcal{A}_j}{S_j^o n L}\right) = \ln(q(T,\nu_0)) - c_2\left(\frac{1}{T} - \frac{1}{T_0}\right)E_i \tag{26}$$

$$q(T,\nu_0) \approx q(T) = \frac{Q(T_0)}{Q(T)}\frac{1-\exp\left(\frac{-c_2\nu_0}{T}\right)}{1-\exp\left(\frac{-c_2\nu_0}{T_0}\right)} \tag{27}$$

As Eq. 26 shows, the number density, n, and pathlength, L, do not need to be known to determine the temperature, as it is solely determined by the slope of the left-hand side versus temperature, i.e. $-c_2\left(\frac{1}{T}-\frac{1}{T_0}\right)$. Typical Boltzmann plot fits are shown in Figs. 9 and 10. The algorithm of York [44] is used to propagate uncertainties in the measured areas and associated linestrengths of the transitions probed to the fitted slope. Once the temperature is determined via the linear fit above, the number density can be determined via equation 7, as $\mathcal{A}_j$, $S(T)$, and L are known.

A rotational temperature can be determined via a Boltzmann regression method provided the states fit lie within the same vibrational band. In this study a majority of the test cases had predicted vibrational relaxation times < 1 μs, however on a few low-velocity test cases T_{rot} was determined via fitting the $\nu_3(01^10)$ R(103), R(104) and R(140) states. These states were chosen over the $\nu_3(00^00)$ states due to greater sensitivity and higher certainty in the measured absorbance areas. The vibrational temperature was estimated through the conservation of stagnation enthalpy shown in

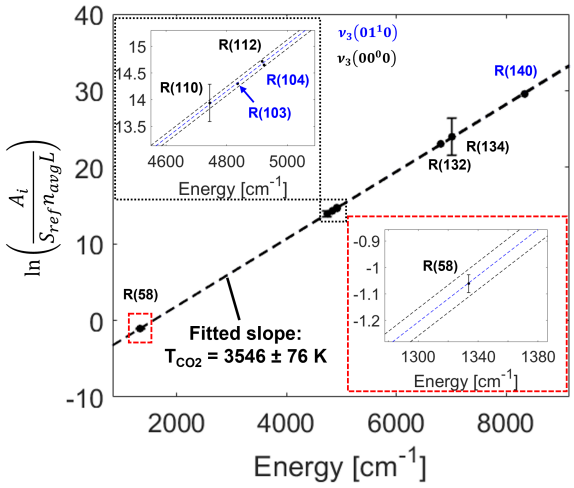

Fig. 9 Multi-line Boltzmann regression of the CO_2 transitions probed in this study on a 1.99 Torr, 3.29 km/s shock at t = 5 μs. Note both the 4.19 and 4.17 μm wavelengths are utilized as all 8 CO_2 features were well resolved on this test. The temperature estimated from the slope is 3546 ± 76 K. Absorbance feature labels in black and blue denote $\nu_3(00^00)$ and $\nu_3(01^10)$ transitions respectively.

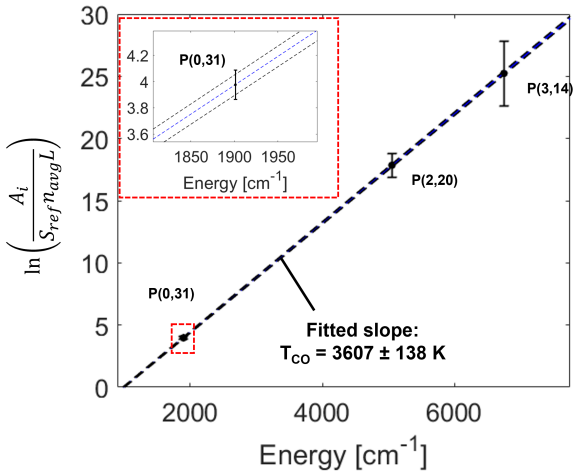

Fig. 10 Multi-line Boltzmann regression of the CO features probed at 4.98 μm in this study on a 1.09 Torr, 3.28 km/s shock at t = 5 μs. The temperature estimated from the slope is 3607 ± 138 K.

Eq. 28. $h_{0,1}$ and $h_{0,2}$ [J/kg] are the stagnation enthalpy before and after the shock passes.

$$h_{0,1} = h_{0,2} = h_f^o(T_{ref}) + C_{p,tr-rot}(T_{rot} - T_{ref}) + h_{vib}(T_{vib}) - h_{vib}(T_{ref}) + \frac{u_2^2}{2} \tag{28}$$

h_f^o [J/kg] is the enthalpy of formation at T_{ref} [K], $C_{p,tr-rot}$ [J/(kg·K)] is the heat capacity at constant pressure, h_{vib} [J/kg] is the enthalpy contribution from the vibrational energy, and u_2 [m/s] is the flow velocity behind the incident shock in the shock fixed frame of reference. Note the flow velocity (u_2) changes during vibrational relaxation by approximately 300 m/s on a majority of the test cases, however this is only attributable to about 3% of the total enthalpy of the flow.

Therefore for this analysis, the vibrationally equilibrated flow velocity is used throughout the test. To calculate $C_{p,tr-rot}$ an expression is given in Eq. 29 which assumes the translational and rotational energy mode are equilibrated (T_{tr} = T_{rot})

$$C_{p,tr-rot} = R + \frac{3}{2}R + \frac{D_{rot}}{2}R \tag{29}$$

R is the gas constant, and D_{rot} is the rotational degrees of freedom (for linear molecules such as CO_2, D_{rot} = 2). Utilizing Eqs. 28 and 29, the vibrational temperature can be estimated on chemically frozen test cases.

IV. Results

Experiments were conducted on the NASA electric arc shock tube (EAST) to reproduce the Mars2020 shock layer environment as measured by the radiometer and nearby thermal plug location on the backshell thermal protection system (TPS). To achieve similarity, three primary fill pressures were used (1.09, 1.49, and 1.99 Torr) and various shock velocities ranging from 1.30 - 3.75 km/s captured multiple points along the flight trajectory. As a result, both chemically frozen and chemically reacting cases were observed. For all but the lowest velocities, vibrational relaxation times predicted by Park [45] and Simpson et al. [46] are on the order of 1 μs. Therefore, given the temporal resolution of the measurement (1 MHz), a 1-temperature spectrum determined from the Boltzmann plot method described in Sec. III is assumed valid over the entire test time, with some exceptions. This section of the paper presents and describes representative results for the test series, while the appendix presents a catalogue of all 52 test conditions with associated absorption data offered as supplementary material. Key comparisons are made in Figs. 11 - 18 between the time-resolved temperatures and species number densities resolved with LAS and the NASA models (DPLR CFD code [47] or LASTA [42]). In the following, the Cruden model will specifically refer to the rate coefficients given in [5]. Time in the lab frame is converted to distance behind the shock front with Eq. 30 where t = 0 is set by the Schlieren spike from the shock front.

$$x = U_{is}t \tag{30}$$

In this work, the boundary layer was considered for tests with shock velocities above 2.5 km/s and only applied to the CO_2 data. CO measurements are expected to be minimally influenced by the boundary layer as the core flow is where CO is being produced. The boundary layer is mostly too cold (<3000 K) to form CO on the timescales of the test, therefore we simply assume no CO is formed in the boundary layer. A second order analysis could include consideration of variable CO formation rates in the boundary layer with varying temperature though that is beyond the scope of this work. Two cases are presented (Figs. 11 and 12) to show the temperature and number densities inferred with and without the boundary layer considered for reference. It is observed that the lower velocity case (2.53 km/s) shows a minimal change in temperature (~<1%) and number density (~<2%) determined with and without consideration of the boundary layer. The higher velocity case (3.4 km/s) shows a much more substantial change in both temperature and

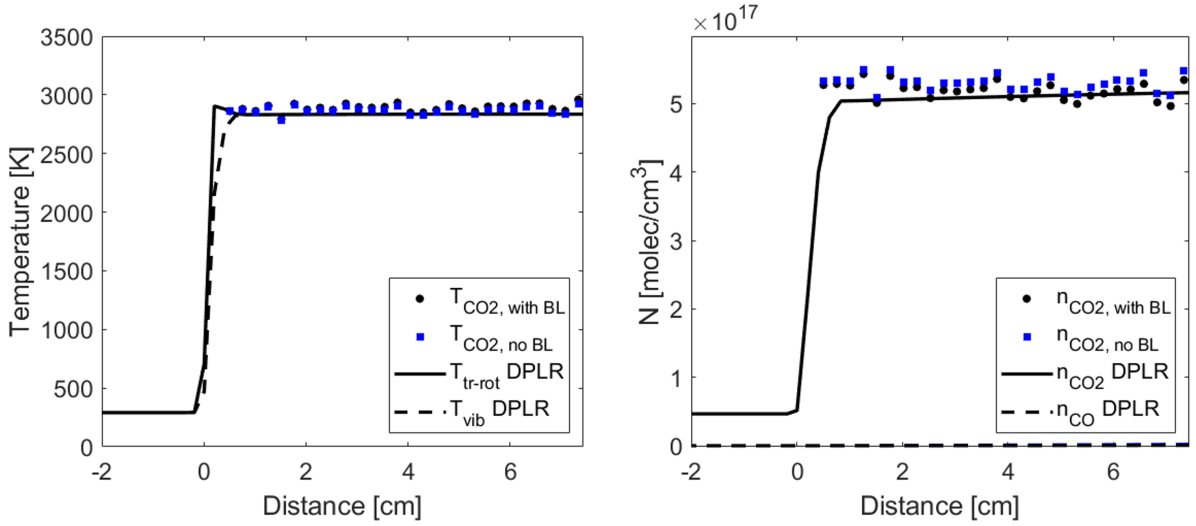

Fig. 11 Temperature (left) and number density (right) vs distance behind shock estimated with (black) and without (blue) the boundary layer for a 2.53 km/s, 1.49 Torr fill pressure test case.

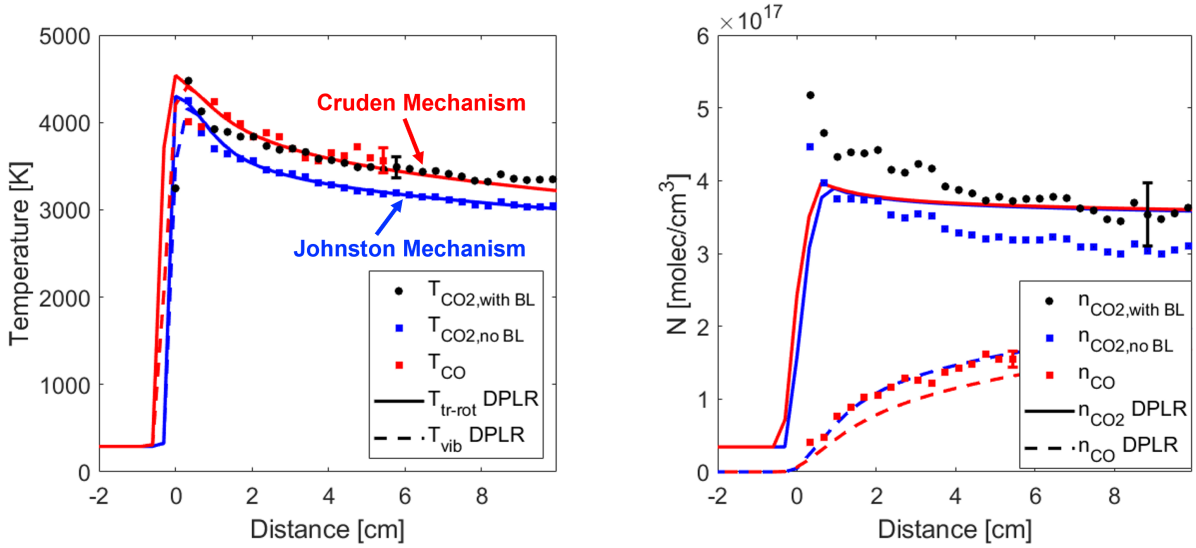

Fig. 12 Temperature (left) and number density (right) vs distance behind shock estimated with (black) and without (blue) the boundary layer for a 3.40 km/s, 1.09 Torr fill pressure test case. CO data becomes optically thick halfway through the test.

number density, on the order of 8% and 15% respectively. Figure 12 also compares the measured temperatures of CO and CO_2, highlighting the better agreement with CO temperature if the boundary layer is accounted. This analysis supports the necessity of considering the compressible boundary layer for shocks at moderate to high velocities (>2.5 km/s) due to the spectral line sensitivity to the cold boundary layer.

Low to moderate velocity results are highlighted in Figs. 13 and 14 and show good agreement with expected values of temperature and number density. On tests with shock velocities below 2.7 km/s, CO_2 dissociation is observed to be frozen during the test time, and thus the simulation is independent of the chemical kinetic mechanism used. The

1.99 Torr fill pressure cases at shock velocities < 2.7 km/s produced a more optically thick spectrum and resulted in slightly higher noise than the 1.09 and 1.49 Torr test cases, though the inferred LAS values showed good agreement with expectations over this velocity range, within ~2% for CO_2 temperature and ~4% for CO_2 number density, and often with closer agreement.

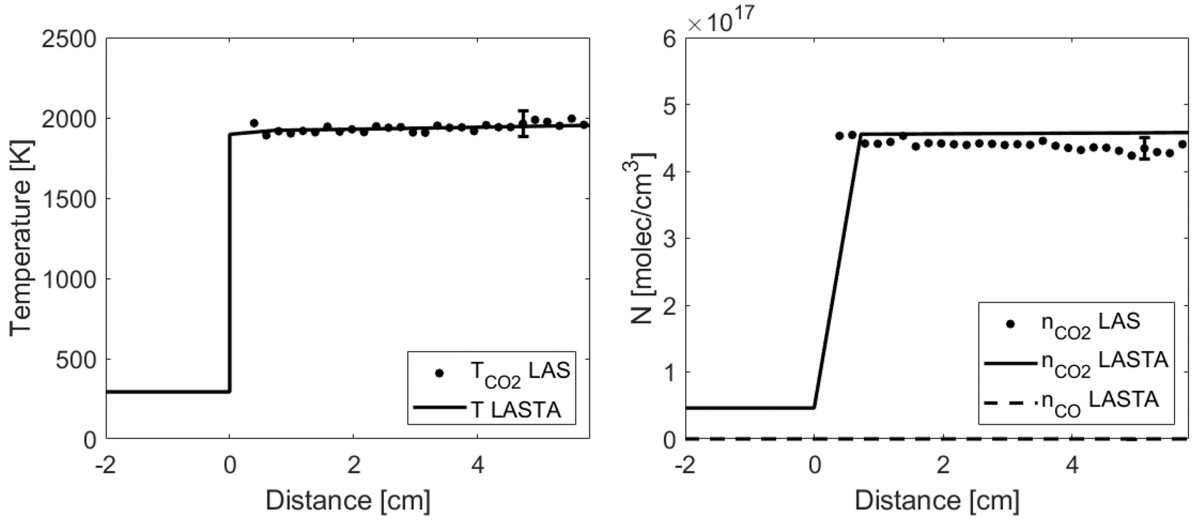

Fig. 13 Spatially resolved temperature (left) and number densities (right) of CO_2. Shock velocity = 1.97 km/s. Fill pressure = 1.49 Torr.

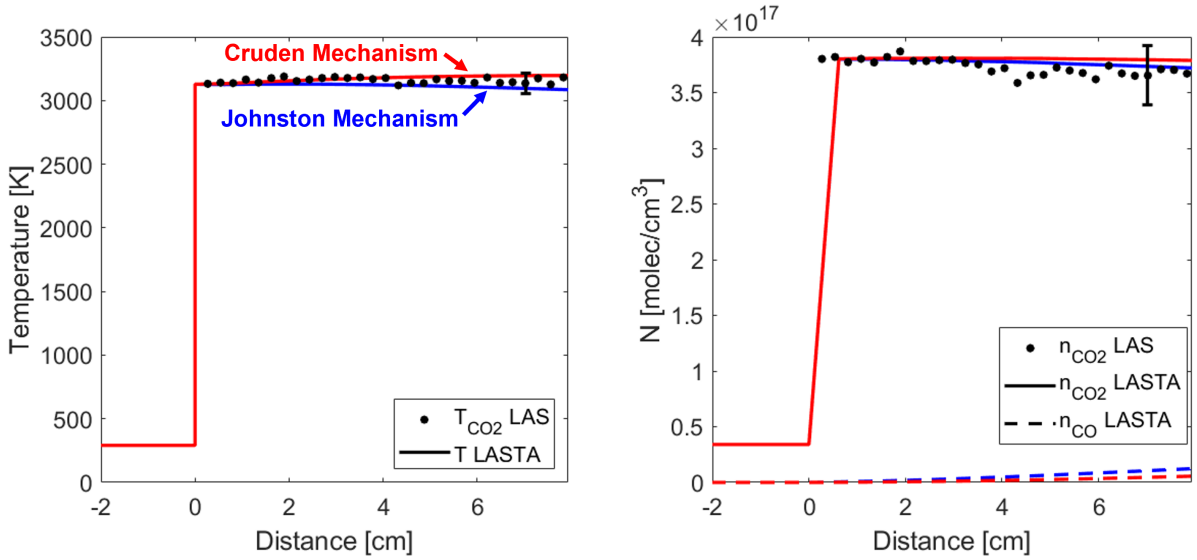

Fig. 14 Spatially resolved temperature (left) and number densities (right) of CO_2. Shock velocity = 2.70 km/s. Fill pressure = 1.09 Torr.

For shocks at moderate to high velocity (≥2.7 km/s), LAS measurements show reasonable agreement between temperatures independently calculated from each species and CFD simulations of the flow. At these velocities, dissociation begins to occur within the test time of the incident shock and the CFD simulation becomes sensitive to the

chemical rate models employed as shown in Fig. 14. Figures 15 and 16 shows the typical inferred LAS temperature and number density trends of the higher velocity cases near and above 3.0 km/s. Again, temperature between CO_2 and CO is mostly found to be within their respective uncertainties and shows a steady decrease as dissociation proceeds. Often CO temperature right behind the shock front is measured to be in slight excess of CO_2 temperature. At these early times or close locations behind the shock, it is challenging to fit the weak CO signal which is further complicated by the overlapping spectrum of CO_2. The measured number density of CO_2 slightly decreases over the test time as an increase in CO number density is observed. Typically the number density of CO_2 is found to be near or in excess of the Cruden mechanism [4, 5] (accounting for the boundary layer), while CO number density is found to more closely follow the Johnston prediction [6], with a number of test results in between the two models. The temperature measurement of CO has a slightly higher uncertainty due to a typically lower SNR in the corresponding spectrum.

Detailed uncertainty analysis is presented in the Appendix and briefly described below. CO_2 temperature and number density uncertainties are found to be 2.4 - 6.5% and 2.6 - 15.9% respectively, with uncertainty in CO_2 number density increasing with shock velocity. The uncertainty in CO_2 temperature decreases as the absorbance of the ν_3 (00^00) R(58) transition becomes less optically thick ($\alpha \rightarrow 1.0$) at velocities above ~2.8 km/s. CO temperature and number density uncertainties are between 3.3 - 4.6% and 5.5 - 8.5% respectively. These results highlight the quantitative nature of the sensor and can be used in model validation efforts.

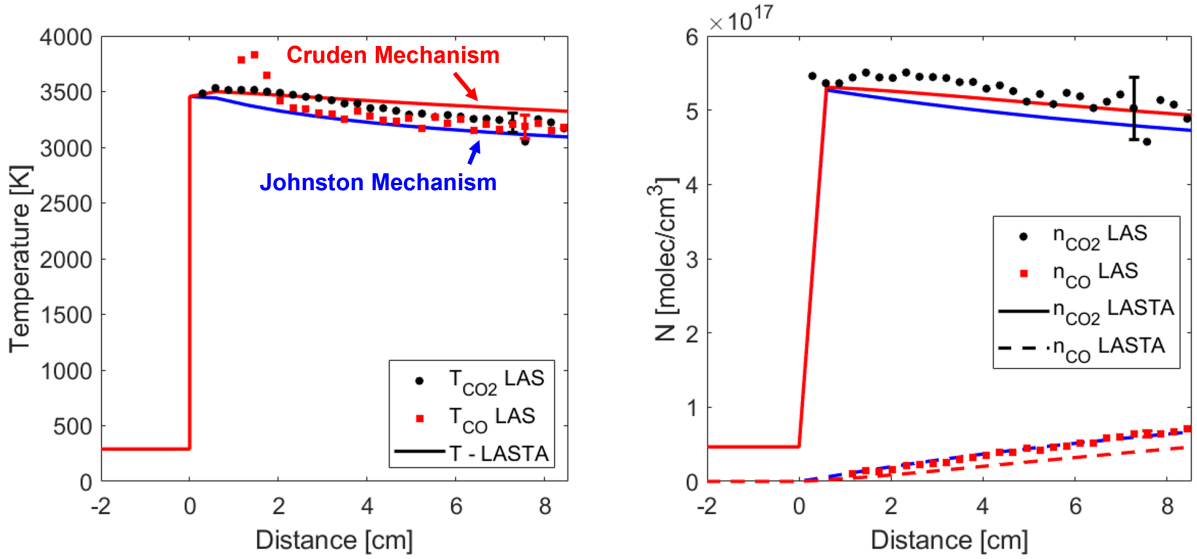

Fig. 15 Spatially resolved temperature (left) and number density (right) for a 2.91 km/s shock with 1.49 Torr fill pressure.

The CO number density results are highlighted in Fig. 17, and resolve a clear trend of increasing CO formation with higher shock velocities as expected. The characteristic formation time of CO is determined by fitting an exponential curve (Eq. 31) to the CO number density and is compared to similar fits of the Johnston [6] and Cruden [4, 5] kinetic

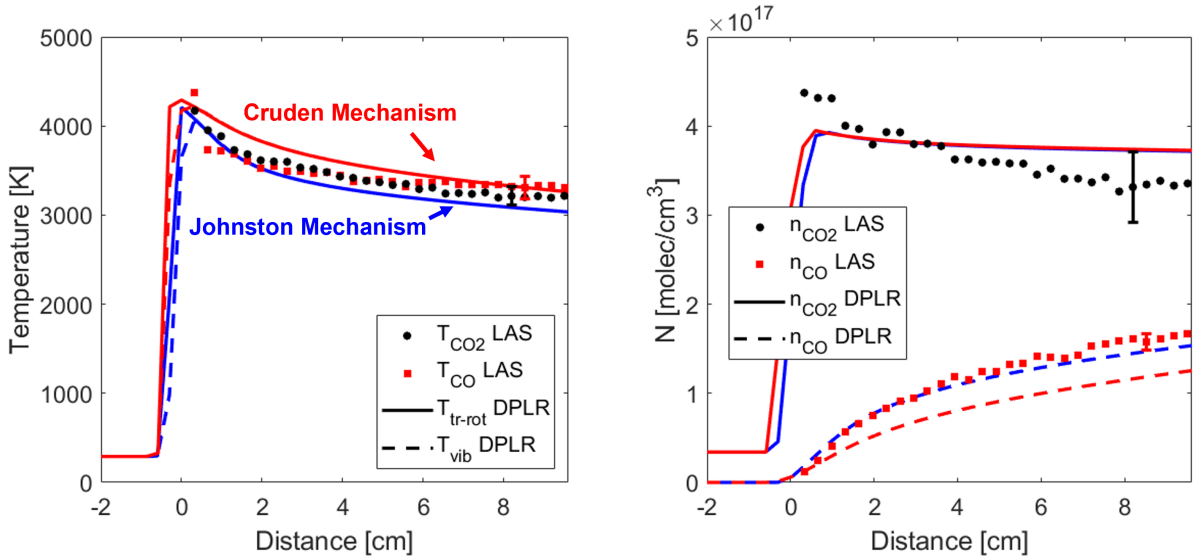

Fig. 16 Spatially resolved temperature (left) and number density (right) for a 3.28 km/s shock with 1.09 Torr fill pressure.

models implemented in DPLR. The particle times were used to determine the characteristic formation times plotted in Fig. 17.

$$n(t) = n_{eq}\left(1 - \exp\left(\frac{-t}{\tau}\right)\right) \tag{31}$$

The CO measurements are found to be mostly in between the two models, trending toward the Cruden [4, 5] model at higher velocities.

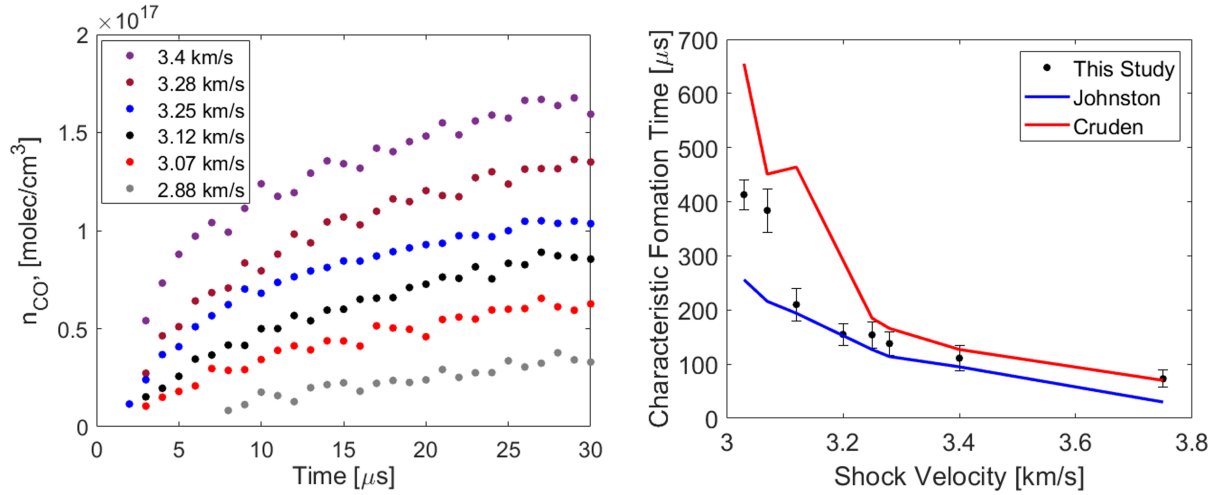

Fig. 17 (left) Measured CO number density with lab frame time for 1 Torr test cases. (right) CO characteristic formation time from measurement and fitted simulations vs shock velocity.

Figure 18 compares the average temperature and CO_2 number density from 2 to 8 cm behind the shock front

predicted from the DPLR and LASTA simulations to the LAS measured quantities for the range of shock velocities covered in this test series. The LASTA model [42] includes consideration of shock deceleration effects and was coupled with the Cantera [48] code to account for flow chemistry. The LASTA–Cantera results are often slightly above DPLR predicted temperatures and lower than DPLR predicted number densities. In a majority of the test cases, the temperature is measured to be within 5% of the Johnston and Cruden models. Number density measurements are typically within 10% of the models and at high velocities (~> 3.3 km/s) tend to be in excess up to 13% for DPLR and up to 30% for LASTA. The LAS results have elevated uncertainties for these high-velocity tests which can be attributed to sensitivity to and uncertainty in the boundary layer size and composition (see Appendix Fig. 20).

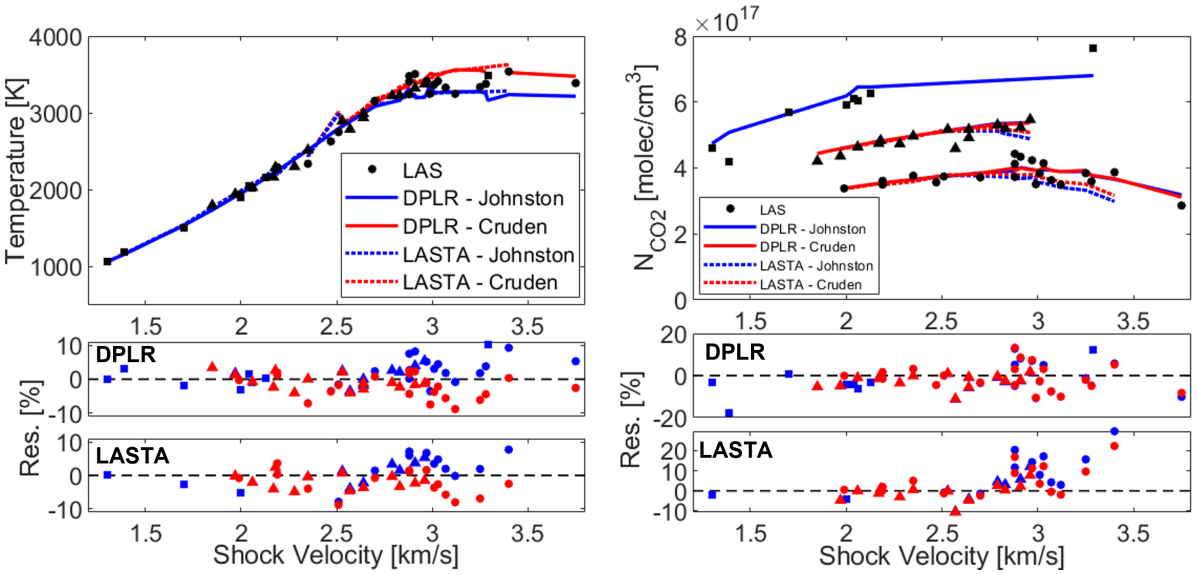

Fig. 18 Measured temperature (left) and CO_2 number density (right) vs shock velocity. Data is compared with the Cruden [4, 5] and Johnston [6] mechanisms simulated in DPLR [47] and the LASTA [42]+Cantera[48] model. Squares, triangles, and circles denote a fill pressure of 1.99, 1.49, and 1.09 Torr respectively.

Lastly, vibrational relaxation was observed on a few low-velocity test cases and a multi-temperature measurement is presented in Fig. 19. This was a low-velocity shock (1.96 km/s) conducted at a fill pressure of 0.49 Torr to observe non-equilibrium between the rotational and vibrational energy modes. Figure 19 shows clear trends from near the vibrationally frozen temperature (~ 3000 K) to the vibrationally equilibrated temperature (~ 1880 K). On some other test cases with velocities at or below 2.1 km/s, and fill pressures at 1.09 Torr or above, the first measurement behind the shock front showed evidence of thermal non-equilibrium between the energy modes, however by the second scan ($t_{labframe}$ = 2 μs), the absorbance was near the equilibrated value precluding a precise measurement of the relaxation time. In the limited tests at low velocities, the vibrational relaxation time measured appears slightly longer than the Park vibrational relaxation model [45] employed in the DPLR code [47].

A complete test catalog of the series is presented as a table in the Appendix and supplemental material is available

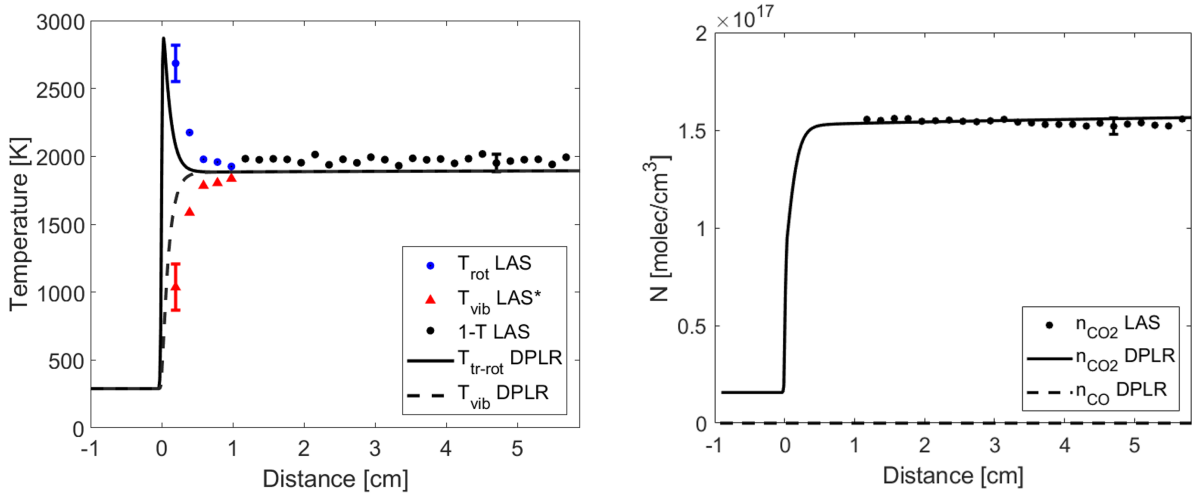

Fig. 19 Time resolved rotational and vibrational temperature shown in blue and red (left) and number density (right) for a 1.96 km/s shock with 0.49 Torr fill pressure. The vibrational temperature is determined from conservation of enthalpy assuming $T_{tr} = T_{rot}$.

containing the absorbance versus wavenumber and time for the corresponding tests on data.nasa.gov.

V. Conclusions

A mid-infrared laser absorption diagnostic has yielded quantitative measurements of temperature and number density of CO_2 and CO at shock conditions relevant to the Mars2020 MEDLI2 heat flux data [1–3]. CO_2 measurements were found to be susceptible to a thin (1 - 2 mm) compressible boundary layer and a numerical simulation was implemented to account for this effect. Independent spectral fitting over CO_2 and CO has yielded similar temperature results and are typically within 5% of the estimated temperature from both the DPLR [47] and LASTA [42] simulation. Number density of CO_2 is found to follow or be in slight excess of the prediction of the Cruden [4, 5] mechanism, with increasing LAS measurement uncertainty as shock velocity increases. The CO characteristic formation time is found to be bounded by the Cruden [4, 5] and Johnston [6] simulations, trending toward the Cruden mechanism at the higher velocities. Average error estimates are found to be 3.7% and 7.1% for temperature and number density of CO_2, and 3.8% and 6.7% for temperature and number density of CO.

In summary, the LAS sensor and method described above and developed over the past two years [8, 9, 49] was successfully deployed on the NASA Ames EAST facility in tandem with optical emission spectroscopy (OES) to measure a re-created Mars entry shock layer to further the investigation of the MEDLI2 flight data and increase the science return of the Mars2020 mission. Overall, the measurement data shows good agreement with predictions using NASA models, and some general consistency with the flight data in that the higher temperature conditions associated with early entry (high velocity) conditions are in better agreement with the Cruden model and lower temperature conditions are in better agreement with the Johnston mechanism. The LAS data and optical emission data are planned for release

on data.nasa.gov and are available for further investigation and comparison to different models. Future experimental studies of the boundary layer size are warranted to assess the accuracy of the simulations and assumptions utilized in this work, though simulations have shown good agreement with an independent code (LASTA [42]). Thermochemical non-equilibrium during Mars entry can be complex, and the data produced in this work and corresponding emission data, detailed in a companion paper [10], can be used together to refine and tune chemical and radiative models underlying predictions of thermal loads during entry to improve design of heat shields for future Mars missions.

Appendix: Uncertainty Analysis

Detailed analysis was performed to quantify the uncertainty in temperature and number density of CO_2 and CO inferred from laser absorption measurements during the Mars2020 MEDLI2 test series (64A) at NASA EAST. This section describes the uncertainty analysis based on the Taylor series method of error propagation which assumes uncorrelated sources of error [50]. Many of the following expressions are well detailed and derived in the appendix of Minesi et al. [43], though this analysis includes an additional term to account for uncertainty from the boundary layer. The non-dimensional uncertainty of a dependent variable r (δr/r) can be calculated from the uncertainty in the independent variables (δx_i) used to calculate r as shown in Eq. 32.

$$\left(\frac{\delta r}{r}\right)^2 = \sum_i \left(\frac{\partial r}{\partial x_i}\frac{\delta x_i}{x_i}\frac{x_i}{r}\right)^2 \tag{32}$$

Temperature uncertainty can be estimated via Eq. 33.

$$\left(\frac{\delta T}{T}\right)^2 = \left(\frac{\delta T_{fit}(\mathcal{A}_j, S_j)}{T}\right)^2 + \left(\frac{\delta T_{BL}(\delta_{99})}{T}\right)^2 \tag{33}$$

The 1σ uncertainty in the linear fit to the Boltzmann plot is output from the algorithm of York [44] and used in Eq. 33. This term is determined considering the uncertainties in the absorbance areas and reference linestrengths. The uncertainty in measured absorbance area A can be estimated via Eq. 34, where α_{pk} is the peak absorbance of the transition [43].

$$\frac{\delta\mathcal{A}}{\mathcal{A}} = \frac{1}{SNR}\left(\frac{\exp(\alpha_{pk})}{\alpha_{pk}}\right) \tag{34}$$

Linestrength uncertainties used in these calculations are shown in Table 2 and are produced from the uncertainty values listed in HITRAN [51], HITEMP [27], and previous work conducted by Jelloian et al. [9]. The $\nu_3(01^10)$ R(140) feature linestrength and uncertainty have been taken from [9] which found R(140) to be on average 8.5% lower than the value listed in HITEMP, though within the tabulated HITEMP uncertainty of 20% [27].

The number density uncertainty is approximated with the expression in Eq. 35, considering the uncertainty in absorbance area, linestrength at the measured temperature, and boundary layer thickness. The derivative of the

Table 2 Linestrength uncertainties used in this work

Molecule	Line Label	δS/S
CO	P(2, 20)	5%
CO	P(0, 31)	2%
CO	P(3, 14)	10%
CO_2	$\nu_3(01^10)$ R(103)	2%
CO_2	$\nu_3(01^10)$ R(104)	2%
CO_2	$\nu_3(00^00)$ R(58)	2%
CO_2	$\nu_3(01^10)$ R(140)	10%
CO_2	$\nu_3(00^00)$ R(134)	10%
CO_2	$\nu_3(00^00)$ R(110)	2%
CO_2	$\nu_3(00^00)$ R(132)	10%
CO_2	$\nu_3(00^00)$ R(112)	2%

linestrength is easily calculated numerically following the evaluation of Eq. 10. The number density uncertainty in this work is evaluated from estimates of the $\nu_3(01^10)$ R(103) line, as this line is neither the strongest nor weakest and well resolved over the range of conditions in this study.

$$\left(\frac{\delta n}{n}\right)^2 = \left(\frac{\delta \mathcal{A}_j}{\mathcal{A}_j}\right)^2 + \left(\frac{\delta S_j^o}{S_j^o}\right)^2 + \left(\frac{1}{S_j(T)}\frac{dS_j}{dT}\delta T\right)^2 + \left(\frac{\delta n_{BL}}{n_{BL}}\right)^2 \tag{35}$$

The boundary layer terms in Eqs. 33 and 35 were evaluated numerically by reprocessing four conditions (as seen in Fig. 20) with a boundary layer thickness adjusted by ± 10% . An estimated 10% uncertainty in boundary layer thickness was chosen upon comparison of the computed boundary layer in this work with that predicted from the LASTA code [42] as shown in Fig. 21. It is observed that the boundary layer contribution to uncertainty grows with shock velocity varying from about 1.5% to 4.3% in temperature and 4.0% to 12.4% in number density.

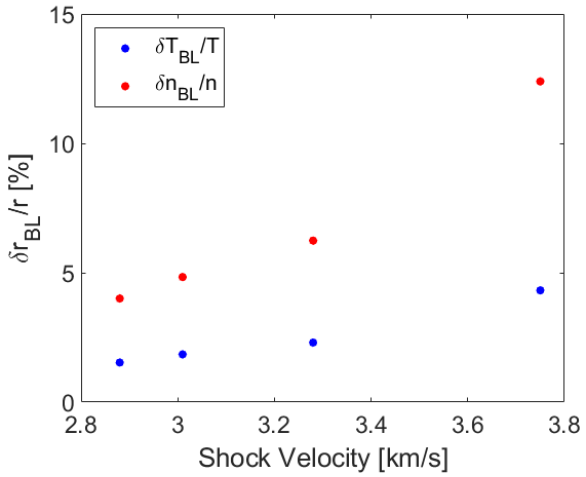

Fig. 20 CO_2 temperature and number density uncertainty from the boundary layer assuming a ± 10% uncertainty to δ_{99}.

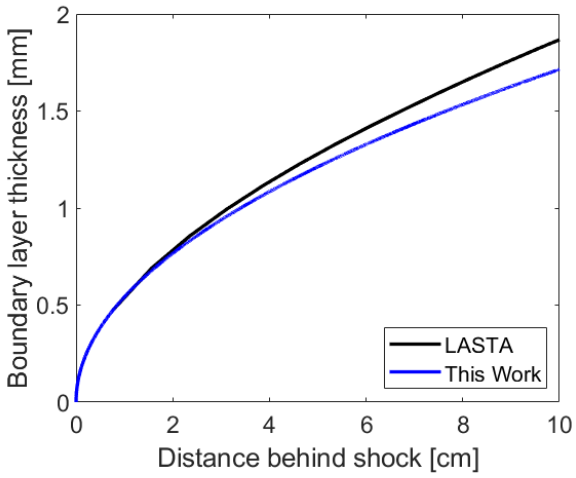

Fig. 21 Boundary layer thickness, δ_{99}, calculated in this work compared to the boundary layer output from LASTA [42] for a 2.91 km/s, 1.49 Torr fill pressure shock.

In this work, the boundary layer was considered for tests with shock velocities above 2.5 km/s and only applied to the CO_2 data. In addition to Fig. 20, Fig. 11 demonstrates the boundary layer correction on a case at 2.53 km/s. The difference in computed temperature and number density at this condition is <1% and 2% respectively. CO measurements are expected to be minimally influenced by the boundary layer where the temperature is too low (<3000 K) to form CO. The core flow is where CO is produced.

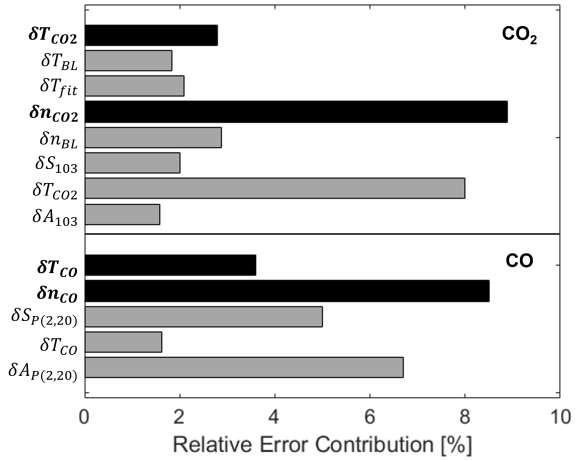

Fig. 22 Bar chart representing the contribution of uncertainty of each term in Eq. 33 and 35 on a 3.01 km/s test case for CO_2 (top) and CO (bottom)

The final uncertainty results were calculated using the method described above and found to be between 2.4 - 6.5 % and 2.6 - 15.9% for CO_2 temperature and number density respectively. CO uncertainties were calculated to be between 3.3 - 4.6% for temperature and 5.5 - 8.5% number density. The sources of uncertainty are highlighted in Fig. 22. CO_2 temperature uncertainty is a combination of both uncertainty due to the fit and boundary layer thickness. The

linestrength sensitivity to temperature is the main contribution to the uncertainty in number density of CO_2. Additionally, as shock velocities increase above $\sim$ 3.4 km/s, the boundary layer begins to significantly affect the CO_2 uncertainty in both temperature and number density. For CO the primary contribution to uncertainty is the P(2,20) area and reference linestrength value for both temperature and number density. In summary, further studies are warranted to drive uncertainties down in reference linestrength values and the size and composition of the compressible boundary layer, however this analysis has shown the LAS sensor has produced quantitative values over the range of conditions investigated in this study.

Appendix: Test Catalogue

Supplemental material is available on data.nasa.gov* and described below in Table 3. The supplemental files contain absorbance vs wavenumber, time (in the lab frame of reference), and distance from the shock front. The table is provided to show the laser absorption data collected throughout this test campaign and test numbers correspond to the companion paper [10] containing the emission data and comparisons between the two diagnostic techniques. The data files are titled <RunNo>_out.mat and contain the following variables (provided the data was collected on the specific test):

- `thisRunNo` = run number
- `CO2_Abs_out_419` = absorbance at 4.19 micron
- `CO2_Abs_out_417` = absorbance at 4.17 micron
- `CO_Abs_out_498` = absorbance at 4.98 micron
- `CO2_WN_out_419` = wavenumber scale corresponding to 4.19 micron [cm^{-1}] absorbance data
- `CO2_WN_out_417` = wavenumber scale corresponding to 4.17 micron [cm^{-1}] absorbance data
- `CO_WN_out_498` = wavenumber scale corresponding to 4.98 micron [cm^{-1}] absorbance data
- `t_labFrame_out` = time in the lab frame of reference corresponding to absorbance scans [μs]
- `x_out` = distance behind shock front corresponding to measured absorbance [cm]

*EAST Test 64: https://data.nasa.gov/docs/datasets/aerothermodynamics/EAST/index.html

Table 3 Summary of LAS data taken during Test64A at the NASA Ames EAST Facility. λ_1 and λ_2 indicate which wavelengths were used during a given test. Test numbers correspond to emission data presented in [10].

Test Number	Fill Temperature [K]	Fill Pressure [Torr]	Shock Velocity [km/s]	λ_1 [μm]	λ_2 [μm]
1	290	1.11	3.20	–	4.98
2	290	1.09	3.25	4.19	4.98
3	291	1.09	3.03	4.19	4.98
4	291	1.09	2.60	–	4.98 - no CO observed
5	–	–	–	–	–
6	291	1.09	2.35	4.19	4.98 - no CO observed
7	294	1.09	2.19	4.19	4.98 - no CO observed
8	290	1.09	2.88	4.19	4.98
9	289	1.09	3.40	4.19	4.98
10	290	1.09	3.07	4.19	4.98
11	290	1.09	2.51	4.19	4.98 - no CO observed
12	287	1.09	2.97	4.19	4.98
13	289	1.09	2.47	4.19	–
14	285	1.09	2.91	4.19	–
15	289	1.09	2.99	4.19	–
16	290	1.09	1.99	4.19	–
17	290	1.09	2.19	4.19	–
18	290	1.09	3.01	4.19	4.98
19	290	1.09	2.88	4.19	4.17
20	291	1.09	2.70	4.19	–
21	289	1.49	2.96	4.19	4.17
22	290	1.49	2.79	4.19	4.17
23	290	1.49	2.57	4.19	–
24	295	1.49	2.17	4.19	4.17
25	293	1.49	1.97	4.19	–
26	291	1.49	2.28	4.19	4.17
27	291	1.49	2.91	4.19	4.98
28	289	1.49	2.64	4.19	–
29	289	1.49	2.53	4.19	4.17
30	291	1.49	2.18	4.19	4.17
31	289	1.49	2.06	4.19	4.17
32	288	1.49	2.64	4.19	–
33	287	1.49	2.83	4.19	4.17
34	291	1.49	1.85	4.19	4.17
35	292	1.49	2.35	4.19	4.17
36	289	1.99	2.00	4.19	4.17
37	287	1.99	2.06	4.19	4.17
38	289	1.99	2.04	4.19	4.17
39	290	1.99	1.39	4.19	4.17
40	290	1.99	1.30	4.19	4.17
41	288	1.99	3.29	4.19	4.17
42	288	1.99	1.70	4.19	4.17
43	292	1.99	2.13	4.19	4.17
44	289	1.09	4.65	4.19	–
45	–	–	–	–	–
46	289	0.49	1.96	4.19	4.17
47	289	1.09	3.12	4.19	4.98
48	288	1.09	2.88	4.19	4.98
49	288	1.09	3.28	4.19	4.98
50	291	8.90	2.02	–	4.98 - no CO observed
51	289	8.90	2.30	–	4.98 - no CO observed
52	291	1.09	3.75	4.19	4.98

Acknowledgments

The authors acknowledge Ramon Martinez, the EAST Facilities staff, and the NASA Ames Entry Systems & Technology Division for their support and technical expertise. The authors acknowledge Anil P. Nair and Kevin K. Schwarm for their expertise in fiber alignment and portable sensor design. Nicolas Q. Minesi acknowledges support from the NASA Space Technology Research Grants Program (award no. 80NSSC21K0066). Christopher C. Jelloian acknowledges support from the NASA Space Technology Research Grants: award no. 80NSSC18K1158 and 80NSSC21K0066.

References

[1] Cruden, B. A., Miller, R. A., Brandis, A. M., Tibere-Inglesse, A. C., Jelloian, C. C., Spearrin, R. M., West, T. K., Johnston, C. O., Prabhu, D. K., Monk, J., Clarke, J., Mare, L. D., and McGilvray, M., "MARS 2020 BACKSHELL RADIATIVE HEATING MEASUREMENT AND SHOCK TUBE VERIFICATION," *9th International Workshop on Radiation of High Temperature Gases for Space Missions*, Santa Maria, Azores, Portugal, 2022.

[2] Miller, R. A., Tang, C. Y., White, T. R., and Cruden, B. A., "MEDLI2: MISP Measured Aftbody Aerothermal Environments," *AIAA SCITECH 2022 Forum*, American Institute of Aeronautics and Astronautics, Reston, Virginia, 2022. https://doi.org/10.2514/6.2022-0551, URL https://arc.aiaa.org/doi/10.2514/6.2022-0551.

[3] Tang, C. Y., Mahzari, M., Prabhu, D. K., Alpert, H. S., and Cruden, B. A., "MEDLI2: MISP Inferred Aerothermal Environment and Flow Transition Assessment," *AIAA Science and Technology Forum and Exposition, AIAA SciTech Forum 2022*, American Institute of Aeronautics and Astronautics Inc, AIAA, 2022. https://doi.org/10.2514/6.2022-0552.

[4] Cruden, B. A., Brandis, A. M., and Macdonald, M. E., "Characterization of CO thermochemistry in incident shockwaves," *2018 Joint Thermophysics and Heat Transfer Conference*, 2018, pp. 1–22. https://doi.org/10.2514/6.2018-3768.

[5] Cruden, B. A., Prabhu, D. K., Borner, A., Meurisse, J., Thornton, J., and Bellas-Chatzigeorgis, G., "Assessment of Fluid Dynamics Boundary Condition in Ablating or Blowing Flows," *AIAA Aviation Conference*, 2023.

[6] Johnston, C., and Brandis, A., "Modeling of nonequilibrium CO Fourth-Positive and CN Violet emission in CO 2 âĂŞN 2 gases," *Journal of Quantitative Spectroscopy and Radiative Transfer*, Vol. 149, 2014, pp. 303–317. https://doi.org/10.1016/j.jqsrt.2014.08.025, URL http://dx.doi.org/10.1016/j.jqsrt.2014.08.025https://linkinghub.elsevier.com/retrieve/pii/S0022407314003690.

[7] White, T. R., Mahzari, M., Miller, R. A., Tang, C. Y., Monk, J., Santos, J. A., Karlgaard, C. D., Alpert, H. S., Wright, H. S., and Kuhl, C., "Mars entry instrumentation flight data and mars 2020 entry environments," *AIAA Science and Technology Forum and Exposition, AIAA SciTech Forum 2022*, American Institute of Aeronautics and Astronautics Inc, AIAA, 2022. https://doi.org/10.2514/6.2022-0011.

[8] Jelloian, C. C., Bendana, F. A., Wei, C., Spearrin, R. M., and MacDonald, M. E., "Nonequilibrium Vibrational, Rotational, and Translational Thermometry via Megahertz Laser Absorption of CO," *Journal of Thermophysics and Heat Transfer*, Vol. 36, No. 2, 2022, pp. 266–275. https://doi.org/10.2514/1.T6376, URL https://arc.aiaa.org/doi/10.2514/1.T6376.

[9] Jelloian, C. C., Minesi, N. Q., and Spearrin, R. M., "High-speed mid-infrared laser absorption spectroscopy of CO2 for shock-induced thermal non-equilibrium studies of planetary entry," *Applied Physics B*, Vol. 128, No. 12, 2022, p. 216. https://doi.org/10.1007/s00340-022-07934-4, URL https://link.springer.com/10.1007/s00340-022-07934-4.

[10] Tibere-Inglesse, A. C., West, T. K., Jelloian, C. C., Minesi, N. Q., Spearrin, R. M., Clarke, J., Mare, L. d., McGilvray, M., and Cruden, B. A., "Reconstruction of Mars2020 Backshell Radiative Heating via Infrared Emission Spectroscopy of CO2/N2/Ar Shockwaves," *AIAA Journal of Thermophysics and Heat Transfer (in review)*, 2023.

[11] Klarenaar, B. L. M., Engeln, R., van den Bekerom, D. C. M., van de Sanden, M. C. M., Morillo-Candas, A. S., and Guaitella, O., "Time evolution of vibrational temperatures in a CO 2 glow discharge measured with infrared absorption spectroscopy," *Plasma Sources Science and Technology*, Vol. 26, No. 11, 2017, p. 115008. https://doi.org/10.1088/1361-6595/aa902e, URL https://iopscience.iop.org/article/10.1088/1361-6595/aa902e.

[12] Grimaldi, C. H., McGuire, S. D., and Laux, C. O., "Infrared emission measurements of a recombining CO2 plasma," *AIAA Science and Technology Forum and Exposition, AIAA SciTech Forum 2022*, 2022, pp. 1–10. https://doi.org/10.2514/6.2022-1782.

[13] McGuire, S. D., Tibère-Inglesse, A. C., Mariotto, P. B., Cruden, B. A., and Laux, C. O., "Measurements and modeling of CO 4th positive (AâĂŞX) radiation," *Journal of Quantitative Spectroscopy and Radiative Transfer*, Vol. 245, 2020, p. 106855. https://doi.org/10.1016/j.jqsrt.2020.106855, URL https://linkinghub.elsevier.com/retrieve/pii/S0022407319308994.

[14] Leibowitz, M. G., and Austin, J. M., "Mid-Wave Infrared Radiation Experiments in Hypervelocity CO2 Blunt Body Flow," *AIAA SciTech 2022 Forum*, AIAA, San Diego, 2022. https://doi.org/https://doi.org/10.2514/6.2022-1783.

[15] Takayanagi, H., Lemal, A., Nomura, S., and Fujita, K., "Measurement of Carbon Dioxide Infrared Radiation in the Afterbody of a Mars entry Capsule," *AIAA SciTech 2017*, AIAA, Grapevine, TX, 2017. https://doi.org/https://doi.org/10.2514/6.2017-1369.

[16] Johnston, C. O., "Evaluating shock-tube informed biases for shock-layer radiative heating simulations," *Journal of Thermophysics and Heat Transfer*, Vol. 35, No. 2, 2021, pp. 349–361. https://doi.org/10.2514/1.T6174.

[17] Cruden, B. A., Prabhu, D. K., and Brandis, A. M., "Measurement and characterization of mid-wave infrared radiation in CO2 shocks," *AIAA AVIATION 2014 -11th AIAA/ASME Joint Thermophysics and Heat Transfer Conference*, American Institute of Aeronautics and Astronautics Inc., 2014. https://doi.org/10.2514/6.2014-2962.

[18] MacDonald, M. E., Brandis, A. M., and Cruden, B. A., "Temperature and CO Number Density Measurements in Shocked CO and CO2 via Tunable Diode Laser Absorption Spectroscopy," *2018 Joint Thermophysics and Heat Transfer Conference*, American Institute of Aeronautics and Astronautics, Reston, Virginia, 2018, pp. 1–23. https://doi.org/10.2514/6.2018-4067, URL https://arc.aiaa.org/doi/10.2514/6.2018-4067.

[19] Wright, M. J., White, T., and Mangini, N., "Data Parallel Line Relaxation (DPLR) Code User Manual Acadia -Version 4.01.1," *Nasa/Tm-2009-215388*, , No. October 2009, 2009, p. 275.

[20] Gnoffo, P. A., "An Upwind-Biased, Point-Implicit Relaxation Algorithm for Viscous, Compressible Perfect-Gas Flows," Tech. rep., NASA Langley Research Center, Hampton, VA, 2 1990.

[21] Whiting, E. E., Park, C., Liu, Y., Arnold, J. O., and Paterson, J. A., "NEQAIR96, Nonequilibrium and Equilibrium Radiative Transport and Sl_etra Program: User's Manual," Tech. rep., 1996. URL https://ntrs.nasa.gov/search.jsp?R=19970004690.

[22] Vargas, J., Lopez, B., and Lino Da Silva, M., "Heavy Particle Impact Vibrational Excitation and Dissociation Processes in CO2," *Journal of Physical Chemistry A*, Vol. 125, No. 2, 2021, pp. 493–512. https://doi.org/10.1021/acs.jpca.0c05677.

[23] Kustova, E. V., and Nagnibeda, E. A., "State-to-state theory of vibrational kinetics and dissociation in three-atomic gases," *AIP Conference Proceedings 585, 620*, 2001. https://doi.org/10.1063/1.1407618.

[24] Kustova, E., Mekhonoshina, M., and Kosareva, A., "Relaxation processes in carbon dioxide," *Physics of Fluids*, Vol. 31, No. 4, 2019. https://doi.org/10.1063/1.5093141.

[25] Kustova, E., and Mekhonoshina, M., "Calculation of vibrational relaxation times in carbon dioxide using forced harmonic oscillator model," *AIP Conference Proceedings*, Vol. 2351, American Institute of Physics Inc., 2021. https://doi.org/10.1063/5.0052238.

[26] Hanson, R., Spearrin, R., and Goldenstein, C., *Spectroscopy and Optical Diagnostics for Gases*, Springer International Publishing, 2016. https://doi.org/10.1007/978-3-319-23252-2.

[27] Rothman, L., Gordon, I., Barber, R., Dothe, H., Gamache, R., Goldman, A., Perevalov, V., Tashkun, S., and Tennyson, J., "HITEMP, the High-Temperature Molecular Spectroscopic Database," *Journal of Quantitative Spectroscopy and Radiative Transfer*, Vol. 111, No. 15, 2010, pp. 2139–2150. https://doi.org/10.1016/j.jqsrt.2010.05.001.

[28] Palmer, G., and Cruden, B. A., "Experimental validation of CO2 radiation simulations," *43rd AIAA Thermophysics Conference 2012*, 2012. https://doi.org/10.2514/6.2012-3188.

[29] Tashkun, S. A., and Perevalov, V. I., "CDSD-4000: High-resolution, high-temperature carbon dioxide spectroscopic databank," *Journal of Quantitative Spectroscopy and Radiative Transfer*, Vol. 112, No. 9, 2011, pp. 1403–1410. https://doi.org/10.1016/j.jqsrt.2011.03.005, URL http://dx.doi.org/10.1016/j.jqsrt.2011.03.005.

[30] Pannier, E., "Conversion of Carbon Dioxide with Nanosecond Pulsed Discharges," Ph.D. thesis, CentraleSupélec - l'Université Paris-Saclay, Gif-sur-Yvette, 3 2019.

[31] Spearrin, R. M., Ren, W., Jeffries, J. B., and Hanson, R. K., "Multi-band infrared CO2 absorption sensor for sensitive temperature and species measurements in high-temperature gases," *Applied Physics B*, Vol. 116, No. 4, 2014, pp. 855–865. https://doi.org/10.1007/s00340-014-5772-7.

[32] Nair, A., Lee, D., Pineda, D., Kriesel, J., Hargus, W., Bennewitz, J., Danczyk, S., and Spearrin, R., "MHz laser absorption spectroscopy via diplexed RF modulation for pressure, temperature, and species in rotating detonation rocket flows," *Applied*

Physics B, Vol. 126, No. 8, 2020, p. 138. https://doi.org/10.1007/s00340-020-07483-8, URL https://link.springer.com/10.1007/s00340-020-07483-8.

[33] Bendana, F. A., Sanders, I. C., Castillo, J. J., Hagström, C. G., Pineda, D. I., and Spearrin, R. M., "In-situ thermochemical analysis of hybrid rocket fuel oxidation via laser absorption tomography of CO, CO2, and H2O," *Experiments in Fluids*, Vol. 61, No. 9, 2020, p. 190. https://doi.org/10.1007/s00348-020-03004-7, URL https://doi.org/10.1007/s00348-020-03004-7.

[34] Nair, A. P., Minesi, N. Q., Jelloian, C., Kuenning, N. M., and Spearrin, R. M., "Extended tuning of distributed-feedback lasers in a bias-tee circuit via waveform optimization for MHz-rate absorption spectroscopy," *Measurement Science and Technology*, Vol. 33, No. 10, 2022, p. 105104. https://doi.org/10.1088/1361-6501/ac7b13, URL https://iopscience.iop.org/article/10.1088/1361-6501/ac7b13.

[35] Cruden, B. A., Martinez, R., Grinstead, J. H., and Olejniczak, J., "Simultaneous vacuum ultraviolet through near IR absolute radiation measurement with spatiotemporal resolution in an Electric Arc Shock Tube," *41st AIAA Thermophysics Conference*, American Institute of Aeronautics and Astronautics Inc., 2009. https://doi.org/10.2514/6.2009-4240.

[36] Trainer, M. G., Wong, M. H., McConnochie, T. H., Franz, H. B., Atreya, S. K., Conrad, P. G., Lefèvre, F., Mahaffy, P. R., Malespin, C. A., Manning, H. L., Martín-Torres, J., Martínez, G. M., McKay, C. P., Navarro-González, R., Vicente-Retortillo, Ã., Webster, C. R., and Zorzano, M. P., "Seasonal Variations in Atmospheric Composition as Measured in Gale Crater, Mars," *Journal of Geophysical Research: Planets*, Vol. 124, No. 11, 2019, pp. 3000–3024. https://doi.org/10.1029/2019JE006175.

[37] Hargis, J. W., and Petersen, E. L., "Shock-tube boundary-layer effects on reflected-shock conditions with and without CO2," *AIAA Journal*, Vol. 55, No. 3, 2017, pp. 902–912. https://doi.org/10.2514/1.J055253.

[38] Petersen, E. L., and Hanson, R. K., "Measurement of Reflected-shock Bifurcation Over a Wide Range of Gas Composition and Pressure," *Shock Waves*, Vol. 15, No. 5, 2006, pp. 333–340. https://doi.org/10.1007/s00193-006-0032-3.

[39] MIRELS, H., "Boundary Layer Behind Shock or Thin Expansion Wave Moving Into Stationary Fluid," *NACA Tech. Note 3712*, 1956.

[40] White, F. M., *Viscous Fluid Flow*, 3rd ed., McGraw-Hill, New York, NY, 2006.

[41] Oz, F., and Kara, K., "A CFD Tutorial in Julia: Introduction to Compressible Laminar Boundary-Layer Flows," *Fluids*, Vol. 6, No. 400, 2021.

[42] Satchell, M., McGilvray, M., and Di Mare, L., "Analytical Method of Evaluating Nonuniformities in Shock Tube Flows: Theory and Development," *AIAA Journal*, Vol. 60, No. 2, 2022, pp. 654–668. https://doi.org/10.2514/1.J060990.

[43] Minesi, N. Q., Richmond, M. O., Jelloian, C. C., Kuenning, N. M., Nair, A. P., and Spearrin, R. M., "Multi-line Boltzmann regression for near-electronvolt temperature and CO sensing via MHz-rate infrared laser absorption spectroscopy," *Applied Physics B: Lasers and Optics*, Vol. 128, No. 12, 2022. https://doi.org/10.1007/s00340-022-07931-7, URL https://link.springer.com/10.1007/s00340-022-07931-7.

[44] York, D., Evensen, N. M., Martinez, M. L., and De Basabe Delgado, J., "Unified equations for the slope, intercept, and standard errors of the best straight line," *American Journal of Physics*, Vol. 72, No. 3, 2004, pp. 367–375. https://doi.org/10.1119/1.1632486, URL http://aapt.scitation.org/doi/10.1119/1.1632486.

[45] Park, C., Howe, J. T., Jaffe, R. L., and Candler, G. V., "Review of chemical-kinetic problems of future NASA missions, II: Mars entries," *Journal of Thermophysics and Heat Transfer*, Vol. 8, No. 1, 1994, pp. 9–23. https://doi.org/10.2514/3.496.

[46] Simpson, C. J. S. M., and Chandler, T. R. D., "A shock tube study of vibrational relaxation in pure CO2 and mixtures of CO2 with the inert gases, nitrogen, deuterium and hydrogen," Tech. rep., 1970.

[47] Wright, M. J., White, T., and Mangini, N., "Data Parallel Line Relaxation (DPLR) Code User Manual Acadia-Version 4.01.1," Tech. rep., 2009. URL https://ntrs.nasa.gov/search.jsp?R=20110006930.

[48] Goodwin, D. G., Moffat, H. K., and Speth, R. L., "Cantera: An object-oriented software toolkit for chemical kinetics, thermodynamics, and transport processes," , 2018. https://doi.org/10.5281/zenodo.170284.

[49] Minesi, N. Q., Blanchard, V. P., Pannier, E., Stancu, G. D., and Laux, C. O., "Plasma-assisted combustion with nanosecond discharges. I: Discharge effects characterization in the burnt gases of a lean flame," *Plasma Sources Science and Technology*, Vol. 31, No. 4, 2022, p. 045029. https://doi.org/10.1088/1361-6595/ac5cd4, URL https://iopscience.iop.org/article/10.1088/1361-6595/ac5cd4https://iopscience.iop.org/article/10.1088/1361-6595/ac5cd4/meta.

[50] Bohm, G., and Zech, G., *Introduction to Statistics and Data Analysis for Physicists*, 2010. https://doi.org/10.3204/DESY-BOOK/statistics, URL http://dnb.ddb.de.

[51] Gordon, I., Rothman, L., Hargreaves, R., Hashemi, R., Karlovets, E., Skinner, F., Conway, E., Hill, C., Kochanov, R., Tan, Y., Wcisło, P., Finenko, A., Nelson, K., Bernath, P., Birk, M., Boudon, V., Campargue, A., Chance, K., Coustenis, A., Drouin, B., Flaud, J., Gamache, R., Hodges, J., Jacquemart, D., Mlawer, E., Nikitin, A., Perevalov, V., Rotger, M., Tennyson, J., Toon, G., Tran, H., Tyuterev, V., Adkins, E., Baker, A., Barbe, A., Canè, E., Császár, A., Dudaryonok, A., Egorov, O., Fleisher, A., Fleurbaey, H., Foltynowicz, A., Furtenbacher, T., Harrison, J., Hartmann, J., Horneman, V., Huang, X., Karman, T., Karns, J., Kassi, S., Kleiner, I., Kofman, V., KwabiaâĂŞTchana, F., Lavrentieva, N., Lee, T., Long, D., Lukashevskaya, A., Lyulin, O., Makhnev, V., Matt, W., Massie, S., Melosso, M., Mikhailenko, S., Mondelain, D., Müller, H., Naumenko, O., Perrin, A., Polyansky, O., Raddaoui, E., Raston, P., Reed, Z., Rey, M., Richard, C., Tóbiás, R., Sadiek, I., Schwenke, D., Starikova, E., Sung, K., Tamassia, F., Tashkun, S., Vander Auwera, J., Vasilenko, I., Vigasin, A., Villanueva, G., Vispoel, B., Wagner, G., Yachmenev, A., and Yurchenko, S., "The HITRAN2020 molecular spectroscopic database," *Journal of Quantitative Spectroscopy and Radiative Transfer*, Vol. 277, 2022, p. 107949. https://doi.org/10.1016/j.jqsrt.2021.107949.